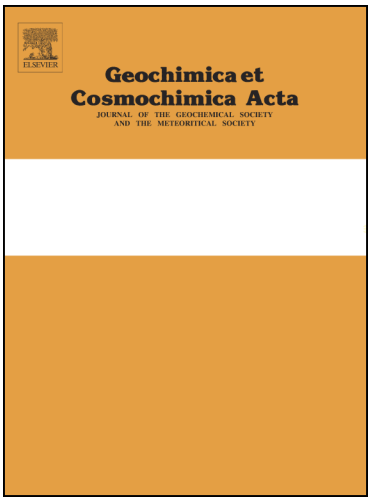

Textural and isotopic evidence for Ca-Mg carbonate pedogenesis

J.L. Díaz-Hernández, A. Sánchez-Navas, A. Delgado, J. Yepes, A. García Casco

PII: S0016-7037(17)30715-9
DOI: https://doi.org/10.1016/j.gca.2017.11.006
Reference: GCA 10545

To appear in: *Geochimica et Cosmochimica Acta*

Received Date: 19 September 2016
Accepted Date: 5 November 2017

Please cite this article as: Díaz-Hernández, J.L., Sánchez-Navas, A., Delgado, A., Yepes, J., García Casco, A., Textural and isotopic evidence for Ca-Mg carbonate pedogenesis, *Geochimica et Cosmochimica Acta* (2017), doi: https://doi.org/10.1016/j.gca.2017.11.006

TEXTURAL AND ISOTOPIC EVIDENCE FOR CA-MG CARBONATE PEDOGENESIS

JL Díaz-Hernández[1], A Sánchez-Navas[2], A Delgado[3], J Yepes[4], A García Casco[2]

[1] *IFAPA, Área de Recursos Naturales, Consejería de Agricultura, Pesca y Medio Ambiente, Junta de Andalucía, 18080 Granada, Spain*

[2] *Departamento de Mineralogía y Petrología-IACT, Universidad de Granada-CSIC, 18071 Granada, Spain*

[3] *Instituto Andaluz de Ciencias de la Tierra CISC-UGR, Armilla, 18100 Granada, Spain*

[4] *Departamento de Ingeniería Civil, IOCAG, Universidad de las Palmas de Gran Canaria, 35017 Las Palmas de GC, Spain*

[*] Corresponding author. *E-mail address*: josel.diaz@juntadeandalucia.es

Abstract

Models for evaluating the terrestrial carbon cycle must take into account not only soil organic carbon, represented by a mixture of plant and animal remains, but also soil inorganic carbon, contained in minerals, mainly in calcite and dolomite. Thick soil caliches derived from weathering of mafic and ultramafic rocks must be considered as sinks for carbon storage in soils.

The formation of calcite and dolomite from pedogenic alteration of volcanic tephras under an aridic moisture regime is studied in an unusually thick 3-m soil profile on Gran Canaria island (Canary Islands, Spain). The biological activity of the pedogenic environment (soil respiration) releases CO_2 incorporated as dissolved inorganic carbon (DIC) in waters. It drives the formation of low-magnesian calcite and calcian dolomite over basaltic substrates, with a $\delta^{13}C$ negative signature (-8 to -6‰ *vs.* V-PDB). Precipitation of authigenic carbonates in the soil is accompanied by the formation of Mg-rich clay minerals and quartz after the weathering of basalts.

Mineralogical, textural, compositional, and isotopic variations throughout the soil profile studied indicate that dolomite formed at greater depths and earlier than the calcite . The isotopic signatures of the surficial calcite and deeper dolomite crusts are primary and resulted from the dissolution-precipitation cycles that led to the formation of both types of caliches under different physicochemical conditions. Dolomite formed within a clay-rich matrix through diffusive transport of reactants. It is precipitated from water with more negative $\delta^{18}O$ values (-1.5 to -3.5‰ *vs.* V-SMOW) in the subsoil compared to those of water in equilibrium with surficial calcite. Thus, calcite precipitated after dolomite, and directly from percolating solutions in equilibrium with vadose water enriched in $\delta^{18}O$ (-0.5 to +1.5‰) due to the evaporation processes.

The accumulation of inorganic carbon reaches 586.1 kg m^{-2} in the soil studied, which means that the carbon sequestration capacity of mafic rocks must be taken into account for certain terrestrial settings. Dolomite together with calcite should be assessed when quantifying carbon stored in arid-semiarid soils as a result of the natural weathering processes.

Keywords: C and O isotopes; C stocks; Caliches; Pedogenic dolomite; Volcanic soils.

1. INTRODUCTION

Geochemical processes occurring in the pedosphere are relevant in the carbon cycle because soils contain both organic and inorganic carbon that must be considered in global carbon budget. Determining the importance of dynamic deep-soil carbon pools is critical for advancing our knowledge of soil-carbon sequestration. Although soil-carbon stocks comprise only a small percentage of the total carbon, such pools contain more carbon than is stored in biomass and in the atmosphere put together (Falkowski *et al.*, 2000; Lal, 2008a). However, considering short residence times of carbon, *i.e.* the real biogeochemical context of global change, after of seawater DIC (dissolved inorganic carbon), terrestrial-pedogenic carbon represents the most important contribution (Sigman and Boyle, 2000; Houghton, 2007).

Sequestration of atmospheric CO_2 by carbonate minerals (mainly carbonate of divalent cations as Ca, Mg, and Fe) represent a real option to mitigate the anthropogenic CO_2 released (*e.g.* Lackner, 2002; Lal, 2008b; Olajire, 2013). Carbon sequestration is a highly dynamic process in humid environments (*e.g.* rain forest), usually with lower pH, because much of the carbon fixed by photosynthesis is released as DIC, DOC (Dissolved Organic Carbon) and particulate organic carbon (Vihermaa *et al.*, 2016). On

the other hand, the efficiency of the immobilization of carbon is critical in arid environments, despite the lower photosynthesis rates, since major amounts of soil inorganic carbon are stored in the form of calcite followed by dolomite. The amounts of carbon stored as pedogenic dolomites in deep soil horizons may be significant, as deduced from the 43 kg m^{-2} on average reached in semiarid areas (Diaz-Hernandez, 2010; Diaz-Hernandez *et al.*, 2013), but it has not generally been measured. Because basic rocks, mainly basalts, have high Ca and Mg contents, the Ca- and Mg-carbonates developed on mafic and ultramafic massifs can be important sinks for carbon storage (Goff and Lackner, 1998; Caldeira and Rau, 2000; Wu *et al.*, 2001; Lackner, 2002; Gysi and Stefánsson, 2011, 2012). The instability of these deep rocks under the conditions of the Earth's surface favours the supply of great quantities of these divalent cations for the precipitation of the carbonate from surface solutions in relatively short times (McGrail *et al.*, 2006; García *et al.*, 2010).

The pedosphere is an essential component of the biosphere and, therefore, the study of the genesis of calcite and dolomite in the soil allows a better understanding of biogeochemical processes which are important for the life on Earth. The enrichment of the lightest C isotope in soil carbonates and the remains of organic matter in arid-semiarid ecosystems results from significant inputs of biogenic carbon derived mainly from C4 plants (Cerling, 1984, 1991). Isotopically light carbon measured in carbonate minerals and graphitized organic matter in direct contact with putative microfossils has been considered as evidence for biological activity on the Earth more than 3,770 million years ago (Dodd *et al.*, 2017). Because of the occurrence of microbial colonies on basaltic glasses and their biotic/abiotic weathering products, the origin of life has been related to alkaline environments derived from basaltic rocks of the primitive Earth (Thorseth *et al.*, 1991, 1992, 1995). In addition, laboratory experiments indicate that

microbial respiration induces the precipitation of diverse Ca-Mg carbonate minerals in saline liquid and solid media (*e. g.* Sanchez-Navas *et al.*, 2009).

The assumption that the same processes operating in nature today have operated in the past does not apply to the case of the dolomite formation, because the abundance of dolomite in ancient rocks contrasts with the scarce dolomite formed in the modern environment. This controversy, together with failure in the efforts to synthesise dolomite in the laboratory under Earth-surface conditions has led to the topic known as the "dolomite problem", and to a debate maintained for decades (*e.g.* Van Tuyl, 1916; Land, 1992, 1998; Arvidson and Mackenzie, 1999). Despite dolomite formation is thermodynamically favourable, stoichiometric, and well-ordered dolomite is formed neither in the aforementioned modern sediments nor in laboratory experiments, because there is a kinetic control of dolomite growth (Krauskopf and Bird, 1995). Instead of ideal dolomite, a Ca-rich and poorly ordered dolomite is formed from some anhydrous Mg-Ca carbonate other than dolomite (Deelman, 2011). Experimental and natural studies of the replacement of calcite by dolomite through interaction with magnesium-rich fluids indicate that the Mg-content and cation order of the protodolomite increases with the advance of the dolomitization process (Kaczmarek and Sibley, 2011).

The formation of authigenic dolomite in relation to the CO_2 enrichment of pedogenic environment of Mg-rich soils is very rare and has been demonstrated only recently by Capo *et al.* (2000), Whipkey *et al.* (2002) and Diaz-Hernandez *et al.* (2013). High Mg:Ca ratios have been reported in soil waters from a neighbouring area of Gran Canaria island, just south of the study area (Gasparini et *al.*, 1990). This favours the incorporation of Mg in Ca-Mg carbonates, which also increase with the substrate age and the progress of the basalt weathering (Whipkey *et al.*, 2002). According to these authors, the presence of clays in the soil profile prevents rapid evaporation of soil water

and facilitates the formation of dolomite. A diffusion-controlled growth of dolomite prompted by the occurrence of clay minerals in the matrix is deduced from the observed textural relations and crystal-growth features in the deeper levels of caliche soils (subsoil) in a semiarid region of SE Spain (Diaz-Hernandez *et al.* 2013).

Mafic rocks weathered under arid conditions to produce Ca-Mg carbonates are evaluated in this study as a potential geological carbon sink. The case investigated involves calcite and dolomite formation from pedogenic alteration of volcanic tephra in an unusually thick 3-m soil profile in the Canary Islands volcanic archipelago. We provide new evidence regarding the conditions of formation of the dolomite. For this purpose, we have made a systematic sampling and a detailed study of the samples taken along the selected profile from the surface horizon to the substrate. We report the occurrence of dolomite as a major mineral in an unusually thick (3 m) soil profile. This study determines: 1) the complete horizon sequence for the soil; 2) mineralogical and compositional changes throughout the profile; 3) the evolution of crystal-growth features, crystallinity, and composition of dolomite with depth; 4) variation of isotopic signature of carbon and oxygen in Mg-carbonates in the profile studied. The distribution of stable isotopes along the profile shows a marked difference in the isotope composition of calcite and dolomite that formed in the soil and subsoil, respectively. More elevated $\delta^{18}O$ values for water near the surface, where calcite formed, resulted from a recharge by meteoric waters accompanied by pervasive evaporation.

2. MATERIAL AND METHODS

2.1. Geological setting and climate

Gran Canaria is an island constituted by several overlapping volcanic edifices of basaltic rocks (Fig. 1A-B), in which the oldest subaerial vulcanism has been attributed

to the Miocene (McDougall and Schmincke, 1976). The island has a well-defined conical shape and its relief is determined by the erosional phases alternating with the magmatic episodes (Fig. 1A, B).

Soils of the study area consist mainly of caliches which fulfil all the requirements of the petrocalcic horizons (Soil Survey Staff, 2014). They are developed primarily near the Gando airport, at an elevation of around 100 m asl, in the eastern sector of the island (Fig. 1A), covering an area of around 45 km^2. In particular, the soil profile studied is located at the eastern slopes of the Roque-Nublo strato-volcano (27º57'53.3''N-15º23'50.8''W; Fig. 1B). This is a gently sloping lava platform, relatively smooth, bounded by east–west trending gullies to the north and south, and dotted with small recent volcanic cones. Most of the coast consists of cliffs 10-30 m high cut on recent volcanics (Fig. 1B).

In the study area the three main subaerial magmatic cycles of the island are represented: Cycle I or Old Volcanics (Miocene); Cycle II or Roque Nublo (Pliocene); and Cycle III, recent or Post-Roque Nublo (Plio-Quaternary) (ITGE, 1990). Figure 1C shows a schematic cross section indicating the spatial relationships between the volcanic materials (magmatic stages) and sediments associated with inactive stages in which erosion was intense, and detritic sedimentation dominated. Recent or Post-Roque Nublo materials consist of massive basanitic lava flows alternating with thinner scoria layers and recent sediments on the top. Locally, some strombolian volcanic cones of fall pyroclastic deposits may be covered by lava flows. They constituted a good aquifer several decades ago but now are mostly drained, except in the southern areas (Cabrera and Custodio, 2004), and thus the water table is located at a depth of almost 100 m in the study area (Fig. 1C).

The caliches were formed from volcanic tephra, probably related to the solidification of lava flows, or from pyroclastic debris deposited during the magmatic episode known as Post-Roque-Nublo cycle (Balcells *et al.*, 1992; Pérez-Torrado *et al.*, 1995). Very scarce fragments of the volcanic tephra appear in the soil profiles, indicating that original volcanic material has undergone an almost complete pedogenic alteration. The beginning of the Post-Roque Nublo cycle has been dated as c. 3.6 My. Volcanic material affected by the pedogenic processes studied here erupted from the NE-SW rift (Carracedo *et al.*, 2002) around 2 My ago (Guillou *et al.*, 2004).

Ages of between 31.2±6.2 and 39±8.8 ky, determined by racemization analyses of gastropod shells (Mangas *et al.*, 2008), have been assigned to the development of the dune field corresponding to the Tufia aeolian deposits that cover the volcanoclastic deposits of the Post-Roque Nublo magmatic phase in the study area. There is no chronological relationship between these aeolian deposits and the beginning of the pedogenic processes responsible of the formation of the caliches studied, the age of which is constrained exclusively by the formation of the volcanic deposits 2 My ago.

Although caliches are relatively old, they must have formed under arid to semiarid conditions very similar to present-day conditions. The trade winds blow with a mean daily wind run of 19909km (SD=6415km), equivalent to a mean annual speed of 27.6 km/h from the north-east of Gran Canaria Island to the south-west. The annual average temperature and precipitation are, respectively, 20-22ºC and 137 mm in the study area, corresponding to warm desert climate (BWh following the Köppen-Geiger classification; Mestre *et al.*, 2012). Extrapolation of soil temperatures reported for the Tenerife Island by Rodríguez et *al.* (2010) and given the conditions of height and orientation of the eastern part of the Gran Canaria Island, a hyperthermic regime can be assigned to the soil studied, according the Soil Taxonomy (Soil Survey Staff, 2014).

Because of these extreme present-day conditions, the vegetation is creeping and scanty, and consists of succulent plants (Bramwell, 1997; Yanes *et al.*, 2008). Most of these plants exhibit CAM (crassulacean acid metabolism) activity, which reduces evapotranspiration during the day, and collects carbon dioxide at night (Pate, 2001).

2.2. Soil morphology and sampling

The study profile represents sections of soil of more than 3 m thick developed from a volcanic tephra (Fig. 2A). The soil appears broadly encrusted by carbonates with a red clayey horizon in the lower levels of the profile, close to the substrate basalt, by means an abrupt contact, which determines the soil drainage in depth. Three main pedogenic levels (petrocalcic horizons), other than the loose surficial horizon (Ap), can be distinguished from the top to the bottom of the profile studied: 1) the Bkkm1 horizon, with a thickness of 1-1.5 m, consists of a massive whitish caliche in places associated with traces of laminar structures on the top (Fig. 2B). 2) A mixed horizon (1 m thick) formed by well-differentiated reddish clayey lenses (Bt) embedded in carbonates (Bkkm2, Fig. 2C). This Bt horizon contains fragments of the precursory volcanic tephra (Vt), which in some cases appear with a pinkish aspect after alteration (PL; pinkish level). 3) A more laminar caliche (Bkkm3) with an irregular thickness (10-50 cm) often fills fissures of the underlying fresh basalts (Fig. 2D).

The fieldwork consisted of studying artificial pits, most of which reached depths of 2-4 m. One representative soil in the locality of El Goro was sampled at intervals of 20 cm from the top to the substratum (300 cm). Sixteen hand samples (c. 1 kg per sample) were collected at 20-cm intervals along the red line in Fig. 2A. In addition, one sample from pinkish levels (PL in Fig. 2C) of the Bkkm2 horizon corresponding to the earliest stages of volcanic tephra alteration and another sample from the basalt of the

substratum were studied. All these samples were air dried. Only a non-cemented soil layer corresponding to the Ap horizon was sieved to extract the fraction <2mm. This fraction and the caliche rocks (0.5 kg per sample) were mechanically homogenized by grinding in a disk mill for 3 or 15 sec, depending of the analytical technique employed. Thus ground powders were prepared for geochemistry, determination of mineralogy, and isotopic analysis. One aeolian dust recovered close El Goro locality was also included in this study to identify the contribution of the allochthonous component of the soils.

2.3. Analytical procedures

2.3.1. Soil-carbon analysis and XRD methods

Soil organic carbon was analysed by the Walkley and Black method (USDA-NRCS 2004) for the 16 samples corresponding to the soil layers studied. The $CaCO_3$ equivalent was measured by a manometric method (Loeppert and Suárez, 1996), using aliquots of c. 0.5 g of homogenized samples and standard. Bulk densities were determined by coating soil fragments of each level with saran resin (USDA-NRCS, 2004) and were measured four times per profile level to compile the representative mean data. The Cm factor (or coarse-fragment material-conversion factor) and carbon content of each level were calculated following the procedures indicated by the Soil Survey Staff (2011). Calcite and dolomite percentages were determined by X-ray diffraction. XRD diagrams of powdered samples were recorded using a PANalytical X'Pert Pro diffractometer (Cu-Kα radiation, 45kV, 40mA) equipped with an X'Celerator solid-state lineal detector. This detector covers an angle of 2.1° and integrates the diffracted intensity over this angle dynamically as it scans. The diffraction patterns were established using a continuous scan between 3 and 50°2θ, with a 0.01°2θ resolution,

~15-min total scan time (equivalent to 20-s counting time per 0.01°2θ). The data were processed using the XPowder® program in order to determine the qualitative and quantitative mineral composition and XRD map (Martín-Ramos *et al.*, 2012). XPowder uses the least-square methods to refine the unit-cell parameters of crystalline phases in order to determine, with the required precision, the exact term of any isomorphic series of minerals. Hence, the molar proportion (mol%) of $CaCO_3$ in Ca-Mg carbonates was determined from *a* and *c* lattice parameter of the rhombohedral carbonate. Lattice distortion associated with Ca-Mg substitution in magnesian calcite-dolomite series was expressed by the measure of the full width at half of the maximum intensity (FWHM) after instrumental broadening and Kα2 corrections. Superlattice reflection peaks were present in the XRD patterns of the dolomite bearing samples, and the degree of cation order in the dolomite lattice was measured by the ratio $I_{(015)}$:$I_{(110)}$ (Goldsmith and Graf, 1958).

2.3.2. Geochemistry and isotopic analysis

Major whole-rock elements were determined by X-ray fluorescence, after fusion with lithium tetraborate. Typical precision was better than ±1.5% for an analyte concentration of 10 wt%. Zirconium was determined by X-ray fluorescence with a precision better than ±4% for 100 ppm Zr. Trace-element determinations were made by ICP-mass spectrometry (ICP-MS) after HNO_3+HF digestion of 0.1000 g of sample powder in a Teflon-lined vessel at ~180°C and 200 psi for 30 min, evaporation to dryness, and subsequent dissolution in 100 ml of 4 vol.% HNO_3. Instrument measurements were conducted in triplicate with a PE SCIEX ELAN- 5000 spectrometer using rhodium as an internal standard. Precision, as determined from standards WSE,

BR and AGV run as unknowns, was better than ±2% and ±5% for analyte concentrations of 50 and 5 ppm, respectively.

Caliche soil samples used for the isotopic study were ground to <200 mesh. Before the isotopic analysis, the samples were heated at 400°C under vacuum for 1 hr to remove the remaining organic matter. About 5 mg of sample was treated with 100% phosphoric acid for 12 h in a thermostatic bath at 50ºC (McCrea, 1950). The samples containing calcite and dolomite were treated according to the method of Al-Aasm *et al.* (1990). This method consists essentially of three steps: 1) obtaining CO_2 after a 2-h reaction with phosphoric acid at 25°C (labelled as calcite); 2) after of 24 h at 25°C elimination of CO_2 from residual calcite and a small quantity of dolomite, and 3) obtaining CO_2 from the continuation of the reaction at 50°C for 24 h that was labelled as dolomite. The carbon dioxide resulting from both methods was analysed using a Delta Plus XP (Thermo-Finnigan) dual inlet mass spectrometer. The experimental analytical error was less than ±0.1‰ for $\delta^{13}C$ and $\delta^{18}O$. The in-house standards Carrara and EEZ-1 were previously verified against NBS-18 and NBS-19. All the samples were compared to a reference CO_2 obtained from a calcite standard prepared at the same time. The oxygen isotope ratios for dolomite were calculated taking into account the fractionation factor for acid decomposition at 50ºC, 1.01057 for dolomite (Rosenbaum and Sheppard, 1986) and at 25°C, 1.01044 for calcite (Kim and O'Neil, 1997).

2.3.3. Electron microscopy and microanalysis

Polished thin sections for petrographic and analytical studies were prepared from 30 soil samples, including at least one from each sample layer and the pink layer (PL), substrate basalt and the red clayey lens (Bt).

Secondary electron (SE) images and energy dispersive X-ray (EDX) microanalyses were performed for soil samples at 60, 100, and 300 cm deep, with a high-resolution field-emission scanning electron microscope (FESEM) Auriga (Carl Zeiss) equipped with a LinK INCA 200 (Oxford Instruments) analytical system.

Soil sample at 60 cm deep was selected for a transmission electron microscopy (TEM) study. It was ground with an agate mortar and the powder suspended in ethanol and deposited in a copper grid. Low-magnification and high-resolution images, selected area electron diffraction (SAED) patterns, single-spot qualitative microanalysis and X-ray elemental maps were made with a FEI TITAN G2 TEM electron microscope operated at 300 kV and equipped with four energy dispersion X-ray (EDX) detectors (SuperX system). Quantitative analytical electron microscopy (AEM) was carried out with a Philips CM20 instrument operated at 200kV and equipped with an EDX model EDAX. Analysis of clay, carbonate minerals and Si-rich amorphous material tightly intergrown with clay and carbonate particles was performed in scanning transmission electron microscopy (STEM) mode using a beam 5 nm in diameter and a scanning area of 20 × 100 nm. For quantitative micro-analyses, EDX data were corrected by the thin-film method of Lorimer and Cliff (1976). The k-factors were determined using muscovite, albite, biotite, spessartine, olivine, and titanite standards.

X-ray elemental maps were made with an electron microprobe CAMECA SX100 for two samples: one from a soil caliche layer located at 60 cm (Bkkm1 horizon) and other from an incipient altered/carbonated volcanic material within clay-rich lenses (pinkish levels of the Bkkm2 horizon; Fig. 2C). Working conditions were 15kV of acceleration voltage, 200 nA of probe current and 3 μm of the spot size. X-ray images were made by moving the polished section sample in a rectangular-shaped area while using a position-fixed beam, and the step-to-step displacement and the acquisition time

were 5 μm and 30 mseg, respectively. After data acquisition, elemental maps and phase maps were made using DWImager software (García-Casco, 2007).

3. RESULTS

3.1. Mineralogical and compositional variation in the soil profile

Calcite and dolomite content (SIC) was determined from the sequence of diffractograms from throughout the study profile (Fig. 3), which shows the evolution from calcite-rich soil caliche layers in the upper levels towards the dolomite-rich caliches in the lower soil layers and dolomite maturation with depth (Fig. 4). Soil organic carbon (SOC) decreases in depth, with the highest content in the horizon overlying the indurated caliche layers (1.25%), and very low quantities throughout the profile (<0.25%), with a monotonic and very slight decline and with no apparent alterations in this evolution (Fig. 4A).

The dolomite and calcite content was quantified by XRD. There is a marked increase of carbonates in depth (Fig. 4B). Calcite concentrates above 180 cm and dolomite shows a smooth increase below 160 cm and was by far the most abundant mineral from 180 cm deep (Fig. 4C). The reverse correlation between calcite and dolomite content was also deduced from the XRD pattern sequence of Figure 3 and grey-scale map in Figure 5. Calcite for a 60 cm sample has low magnesium content (X_{Mg}^{Cal} = 0.080). Dolomite will be referred to hereafter as calcian-dolomite because it is not a stoichiometric phase, with X_{Mg}^{Dol} ranging from 0.40 (0-160 cm) to 0.48 (180-300 cm) as determined from the unit-cell parameters (Fig. 4D, Table 1) and confirmed by the AEM analyses of the TEM study (see below). Superstructure reflection (*015*) observed in well-ordered dolomites (Goldsmith and Graf, 1958; Reeder and Sheppard, 1984) appeared in the dolomite-rich samples of the lowest levels. Higher values of the

$I_{(015)}$:$I_{(110)}$ ratio were found for the dolomite occurring below 160 cm deep, indicating a higher degree of cation order in the dolomite lattice with depth (Fig. 4E, Table 1). Crystallinity of the dolomite, negatively correlated with FWHM, increased with depth (Fig. 4F, Table 1). Therefore, the most crystalline, ordered, and near-ideal stoichiometric dolomite occurred at the deepest levels in the profile.

In addition to calcite and dolomite, the mineralogy of the soil samples determined by XRD also consisted of sepiolite, palygorskite, and quartz (Fig. 3). As expected, caliche soil samples contained low amounts of clay minerals and quartz, with the exception of sample at 60 cm deep with a high sepiolite content. The distribution of the silicate minerals in the profile studied was investigated in the decarbonated samples analysed by Cuadros *et al.* (2016), who held that the occurrence of silicate phases in the caliches diminish with depth. Palygorskite is most abundant in the lower part of the profile. It progressively decreases upwards and disappears in the upper caliche layers. Sepiolite occurs only in the Bkkm1 horizon and disappears below 160 cm. The Ap horizon was particularly rich in quartz.

Together with carbon, the most abundant elements in the study profile were Ca and Mg, their content being controlled by the distribution of calcite and dolomite. Specifically, from 180 to 300 cm the CaO and MgO content were, respectively, 30 and 20%, *i.e.* very close to those of the dolomite (Fig. 6A). The high CaO content to 180 cm deep is explained by the calcite of the Bkkm1 horizon, so that the CaO pattern mimics that of calcite in this part of the profile. Ca and Mg were scant both in the upper (Ap horizon) and lower parts (substrate) of the profile. On the other hand, silica registered two high values corresponding to the Ap horizon (35%) and the basaltic substrate (41%), with a decreasing trend (ranging between 15.5 and 3.7%) from 20 to 300 cm (Fig. 6B). An atypical Si and Mg enrichment was detected at 60 cm deep (26.1% and

16.5%, respectively), corresponding to the sample particularly rich in sepiolite (Fig. 3). Aluminium, iron, sodium, and potassium oxides gently increased from 20 to 220-240 cm, with high values in Ap horizon and basalts (Fig. 6B and C). Altered volcanic tephra with pinkish aspect (pinkish level, PL sample) had the lowest content in CaO (1.7%; Fig. 6A and Table S1) and the maximum value of SiO_2 (more than 50%; Fig. 6B). It also showed high Fe_2O_3 (6.2%), TiO_2 (1.5%), and K_2O (1.2%). Highest iron content was found in the fresh basalt of the substrate (13.7%; Fig. 6B and Table S1).

Transition metals (Ti, V, Cr, Ni, and Cu), high field-strength elements (HFSE, Zr in particular) and rare-earth elements (REE) followed a similar pattern (Table S1; Fig. 6D - F). Therefore, a smooth increase in the content of trace elements was observed with depth, in particular for HFSE, Zr, and REE. The reworked Ap horizon, basaltic substrate, PL sample, and aeolian dust were characterized by high trace-element contents (Fig. 6D - F).

3.2. Distribution of carbon and oxygen isotopes throughout the soil profile

The distribution of $\delta^{13}C$ and $\delta^{18}O$ values of the carbonates in the upper part of the profile is controlled by the calcite of the Bkkm1 horizon, whereas the lower part of the curves mimics the distribution of $\delta^{13}C$ and $\delta^{18}O$ in dolomite, which is the most abundant carbonate mineral in the lower Bkkm2 and Bkkm3 levels (Fig. 7). The distribution of $\delta^{13}C$ of the carbonate minerals (calcite+dolomite) throughout the profile varies from -8.67 in the upper part of the Bkkm1 horizon to -6.15‰ (V-PDB) in the lowest level (Bkkm3 horizon; Table S2). The behaviour of the $\delta^{13}O$ of the carbonate minerals throughout the study profile is very similar to the carbon, ranging from -2.09 in the upper part of the Bkkm1 horizon to -0.19‰ (V-PDB) in the Bkkm3 horizon (Table S2). These $\delta^{13}C$ and $\delta^{18}O$ values are relatively constant for the deeper Bkkm1

and Bkkm3 horizons. In the upper levels of the profile where isotopes values are present for calcite and dolomite, $\delta^{13}C$ and $\delta^{18}O$ values are more negative for calcite (Fig. 7A and Table S2; mean values between -6.56‰ and -0.82‰, respectively) than for dolomite (Fig. 7B and Table S2; mean values are -6.25‰ and -0.43‰, respectively).

3.3. Textural relations, dolomite crystal growth features and composition of carbonate minerals

3.3.1. SEM and TEM study

SE images show complex textural relations between carbonates and clay minerals (Fig. 8). Fine-grained aggregates of rounded calcite nanocrystals of a few hundred nanometres in size appear tightly intergrown with subhedral rhombohedra of calcian dolomite with sizes less than 1 μm within the Bkkm1 horizon (Fig. 8A). There are also sepiolite fibres that seem to post-date the formation of the carbonate. The occurrence of calcian dolomite rhombohedra within sepiolite and/or palygorskite mats was observed throughout the profile, regardless of the depth. Sometimes no clear limit was discerned between calcian dolomite rhombohedra and the sepiolite and palygorskite fibres coating the surface crystals (Fig. 8B). Below 200 cm in depth, calcian dolomite rhombohedra aggregated, forming spherulitic morphologies (Fig. 8C) with very small fibres on their crystal surface (Fig. 8D).

Crystal morphology of calcian dolomite varied with depth throughout the study profile: no planar surfaces were detected in the calcian dolomite in the upper levels of the profile, whereas skeletal crystals appeared at intermediate depths and well-shaped rhombohedra formed below 200 cm (Fig. 8D).

Samples at 60 cm, characterized by the presence of a calcian dolomite of low crystallinity as determined by the XRD study, were analysed in detail by TEM. The

small rhombohedra displayed in Figure 9A-B (with edge length around 200nm) were formed during the grinding process for the sample preparation, because of skeletal crystals found at this depth resulted from an aggregation-based crystal-growth mechanism (see Fig. 8C) and dolomite showed perfect rhombohedral exfoliation. The low-magnification image of Figure 9A shows sepiolite fibres together with the idiomorphic calcian dolomite particle. Elemental X-ray maps reveal: 1) Mg and Si-content at the boundaries of the calcian dolomite rhombohedra that correlate with separate sepiolite grains and with a Si-rich undetermined materials on its surface (Fig. 9C and E; see also below); 2) the high Ca and Mg content and the absence of Si within the idiomorphic carbonate particles (Fig. 9D-E). Low crystallinity deduced from the previous XRD studies consists of crystalline imperfections visible under TEM: crystalline mosaicity results in a patched contrast, variable orientation of the lattice fringe in the diverse mosaic blocks (Fig. 9F) and a spongy appearance for the single crystal in low-magnification TEM images (Fig. 9B). Diffraction rings defined by diffraction spots (Fig. 9G) indicate that mosaic blocks forming calcian dolomite rhombohedra are not well aligned (*i.e.* the diffraction for each block is not completely contiguous with that from all other blocks). These small idiomorphic particles were firmly identified as carbonates (dolomite) by EELS (Fig. 9H): 1) ELNES of C-*K* edge corresponds to those of CO_3^{2-} anion, and spectral features of Ca-$L_{2,3}$ and O-*K* fine structures are typical to those of rhombohedral carbonates; 2) presence of a peak at the Mg-*K* edge.

The AEM analyses of the carbonate minerals from the sample at 60 cm in depth indicate the occurrence of a Ca-rich dolomite (X_{Ca}=0.68) at this depth, which coexist with a magnesian calcite (X_{Mg}=0.10, Table 2). X_{Mg} from AEM analyses of the calcian dolomite from 160 cm in depth is 0.39, clearly higher than that of the sample at 60 cm

(X_{Mg}=0.32, Table 2). The frequency histogram of the X_{Mg} content determined by AEM for samples at 60 and 160 cm shows a bimodal distribution (Table 2A). The narrow peak at low X_{Mg} values and the peak with an asymmetric shape skewed to the left located at higher X_{Mg} values correspond, respectively, to the low Mg-calcite and calcian dolomite determined by XRD. The X_{Mg} values provided by AEM analyses are lower than those derived from the unit-cell refinement (compare Tables 1 and 2B). In both cases, the calcian dolomite from lower depths had a lower Mg content compared to more ideal stoichiometric dolomite from deeper levels in the profile.

3.3.2. EPMA study

X-ray elemental maps of caliche samples at 60 cm deep show a wide compositional range for the Ca- and Mg-carbonates, distinguishing the diverse carbonate minerals (calcite, dolomite) and associated clay minerals (sepiolite, palygorskite, smectite; Figs. 10 and 11). These caliches are formed by rounded concretions of Ca-dolomite and sepiolite tightly intergrowth, with minor calcite in the inner part of some grains (Fig. 10A). The Ca-Mg-Si triangle in Fig. 10B contains the analyses showing an intermediate composition between dolomite (compositional field 1 in Fig. 10B) and calcite (compositional field 4 in Fig. 10B). Thus, compositional fields 2 and 3 defined by the intermediate pixels extending along the Ca-Mg edge can be assigned to Ca-dolomite and Mg-calcite, respectively.

The false colour of Mg X-ray (Kα) distribution maps of Figure 10C-D also distinguishes the spatial distribution of these mineral phases. Thus, it can be appreciated that the dolomite (1; red) occurs directly in contact with the Ca-dolomite (2; yellow/green colour) both within sepiolite-rich areas (white) of the matrix (arrows) and at the rims of the rounded concretions.

The phase map made for the pinkish levels located at 2 m deep within the Bkkm2 horizon (PL sample) shows the occurrence of abundant clay minerals (smectite, palygorskite+sepiolite, Mg-sepiolite) with minor carbonates (exclusively dolomite) and quartz (Fig. 11). The increase in quartz content with depth in the study profile has been broadly documented in a previous work performed on decarbonated samples by Cuadros *et al.* (2016). These authors also showed that the smectites are located preferentially within the remains of the precursory volcanic tephra; whereas palygorskite and sepiolite constitute mainly the altered matrix, which is also evidenced in our Figure 11A. Dolomite is the result of a scant carbonatation of the altered volcanic tephra and appears restricted to pores and vacuoles, where it coexists with Mg-sepiolite in some cases.

4. DISCUSSION

4.1. Mineral authigenesis and geochemical processes in the soil

Dolomite constitutes some 90% of the soil material below 180 cm and calcite almost 40% above this depth, with a region of coexistence of these two Ca-Mg carbonates at 60 to 160 cm in depth (Figs. 4B, C). The high abundance of dolomite and calcite in the soils studied implies a large supply of DIC during the weathering of the volcanic deposits together with the incorporation of Ca into the system. This is deduced from Figure 6A, which shows that the Ca content in the soil profile is markedly higher than in the basalt substrate (with chemical composition similar to that of the original volcanic tephra). Ca-Mg carbonates of the soil profile were derived from the weathering of silicate rocks rich in magnesium and calcium via reactions that may be summarized by the well-known Urey reaction (Urey, 1952):

$$\text{Ca/Mg-silicate} + CO_2 \rightarrow \text{Ca/Mg-}CO_3 + SiO_2 \qquad (1)$$

According to Reaction 1, carbonatation of the basaltic volcanic tephra released silica, which would explain the SiO_2 enrichment between 40 and 80 cm deep (Fig. 6B). The redistribution of elements such as Si, Ca, and Mg in the profile (Fig. 6A, B) is associated with the precipitation of dolomite, calcite, palygorskite, and sepiolite along the diverse areas of the profile (Fig. 4 and Cuadros *et al.*, 2016). As suggested above, part of the Ca necessary for the formation of the dolomite at lower levels and the calcite of the upper levels in the profile was supplied together with DIC by the descending meteoric water. Therefore, the overall reaction, also including the precipitation of sepiolite in the upper levels, can be written by the following reaction (unbalanced for oxygen):

$$12SiO_4Mg_2 + 33CO_2 + 2H_2O + 17CaO \rightarrow 16CaMg(CO_3)_2 + Si_{12}O_{30}(OH)_4Mg_8 + CaCO_3 \quad (2)$$

In relation to this Ca supply to the soil, some authors have cited aeolian dust as the main source of calcium for the formation of calcretes and dolocretes from the Canary Islands (Huerta *et al.*, 2015, Alonso-Zarza *et al.*, 2016). Calculation of tau (τ) values for Si, Ca, and Mg indicates very minor or no contribution to soil by aeolian dust monitored here using the Ap horizon of the soil profile (Fig. 12). The aeolian contribution has only a small significance in the case of the Ap horizon where aeolian quartz has been found, and a high content of trace element is observed (see end of this section).

The progress of the alteration process and the massive precipitation of dolomite, calcite, and sepiolite throughout the profile (Fig 6B-F) drastically diminished the content of chemical elements such as Ti, Al, Fe, K, Na, HFSE, REE, and LILE in the soil profile with respect to the basalt substrate and the Ap horizon due to the dilution of these elements. Iron was particularly abundant in soil samples affected by minor

carbonatation (sample PL in Table S1 and Fig. 6B; Fig. 9 in Cuadros *et al.*, 2016). Despite the low quantities of Ti, Al, Fe, HFSE, and REE in carbonated samples, they seem to be slightly concentrated in the lower horizons of the soils (Table S1 and Fig. 6B-F). These elements are not easily released from the basaltic parent-rock. In the study case, Na, K, and LILE were fixed in smectite, where they are essential structural components (Na and K), or trace elements that replace Na and K (LILE; Cuadros *et al.*, 2016). This explains their abundance in the less-carbonated soil samples (*i.e.* sample PL). Oxidation of Fe quickly fixed the iron released from Fe-rich parent rocks in iron oxyhydroxides or in the structure of nontronite and Fe-rich montmorillonites (Cuadros *et al.*, 2016). The small increase of practically all trace elements in the lower levels of the soil profile close to the basaltic substrate can be explained by the occurrence in these horizons of non-altered accessory minerals of the parent rock containing these elements, which remain incorporated in oxyhydroxides and clays formed during the early stages of weathering.

The aeolian dust is characterized by relatively high content of trace and rare-earth elements, close to those of Ap horizon and basalt substrate (Figs. 6D-F, Table S1). This is interpreted as due to the incorporation of some aeolian (allochthonous) components to this horizon. The similarity between the trace-element distribution in the substrate basalts and Ap horizon can be explained by the redeposition of the soil material in the Ap horizon as the result of anthropic reworking. However, the high content of trace and rare-earth elements in the Ap horizon may also result from local contribution to soil by the wind-borne dust, as deduced by the presence of aeolian quartz in this horizon (Fig. 4 and Menéndez *et al.*, 2007).

4.2. Paragenetic sequence in mineral formation

Field and experimental evidence indicates that the rate of the overall reaction including the carbonatation and the hydration of volcanic material is limited by the release of cations from silicate minerals (Gislason *et al.*, 2010). In the present case, transformation of magnesium silicates to carbonates was preceded by hydrolysis affecting the volcanic material. During this early process, Mg orthosilicates of basalts such as forsterite reacted with water to form dissolved silicic acid and bases (Mg, OH), and finally to form Mg-rich clay minerals. This explains the abundance of sepiolite and palygorskite in less carbonated samples (*e.g.* PL sample, Fig. 11). Minor smectites and quartz also formed in the pinkish level corresponding to a less carbonated volcanic tephra. The sample, located at depth in the profile, represents one of the earliest stages of alteration in the soil profile. It contains key secondary phases such as palygorskite, smectite, and quartz as the major constituents of early paragenesis (see Figs 10 and 11 in Cuadros *et al.*, 2016). After this first stage, minor dolomite and later sepiolite were produced, as also observed in the PL sample. The occurrence of major quantities of palygorskite, quartz, and smectite in decarbonated samples from the lower part of the profile was interpreted by Cuadros *et al*. (2016) as result of conservative weathering processes (*in situ* alteration of the volcanic tephra); whereas the major content of sepiolite and calcite in the upper level was interpreted in relation to an input of Si, Ca, and Mg at the top (Fig. 12). The formation of quartz, smectite, and palygorskite, resulting from *in situ* alteration of the volcanic tephra, preceded the massive dolomitization occurring in lower horizons. Accordingly, the proposed sequence is as follows: smectite+quartz, palygorskite+dolomite, sepiolite+calcite.

4.3. Carbon and oxygen isotopes as indicators for environments and processes

Stable isotopes can provide information related to an authigenic or inherited origin of dolomite in soils. The $\delta^{13}C$ values (from -9 to -6‰) are typical of the carbonates formed in meteoric environments (Salomons and Mook, 1976; Salomons *et al.*, 1977; Deines, 1980). The most negative $\delta^{13}C$ values were found in the calcite and dolomite of the upper soil levels (around -8‰, Fig. 7A). The $\delta^{13}C$ values measured in dolomite (Fig. 7A and Table S2) are also consistent with a pedogenic origin, in relation to CO_2 respiration from plants exhibiting CAM photosynthesis (Fig. 13) or a mixing of C3 and C4 plants. CAM plants have a broad range of $\delta^{13}C$ values of around -17‰ (Quade and Cerling, 1990). The CO_2 released (plant respiration and soil-microbe respiration) has a similar isotope composition as the biomass of plant cover. Because degasification processes provoke isotope fractionation, the resulting isotope composition of the CO_2 in the soil is about 4.5‰ heavier than that of the CO_2 released by the plant biomass (Cerling, 1984; Cerling and Hay, 1986; Quade *et al.*, 1989). Fractionation between CO_2 and DIC is relatively constant and dependent on temperature for neutral and basic pH, and the carbonates precipitated in equilibrium with DIC are enriched about 1‰ (Emrich *et al.*, 1970; Friedman and O'Neil, 1977; Usdowski and Hoefs, 1993; Romanek *et al.*, 1992). Given an average temperature of 21ºC, the carbonates studied are enriched by 9.5‰ with respect to the pedogenic CO_2. Consequently, the average values of $\delta^{13}C$ carbonates of -6.8‰ indicate a pedogenic CO_2 of about -16.3‰, and an average for the plant cover of -20.8‰ (V-PDB), implying a mixing of C3 and CAM (and/or C4) plants (Fig. 13), in agreement with the present biomass (Bramwell, 1997; Yanes *et al.*, 2008). In fact, Gasparini *et al.* (1990) report $\delta^{13}C$ in DIC for groundwater of Gran Canaria between -7.1‰ and -15.9‰ (V-PDB). A contribution of atmospheric CO_2 can also be considered. A single contribution to

carbonates in soil from the atmospheric CO_2 would give positive values (Fig. 13). However, even in desert areas, the pCO_2 from soil respiration is relatively high *vs.* the atmospheric component (Cerling, 1991). In summary, the occurrence of CAM and C4 plants would account for the isotopic values found here. The homogenous $\delta^{13}C$ values found in depth, and associated with the formation of dolomite, is explained by the homogenization of the DIC in the subsoil, this being consistent with an authigenic origin for dolomite.

On the contrary, carbonate spring deposits from this area (Gran Canaria Island) related to carbon depth show positive $\delta^{13}C$ values of +2.63 to +4.29‰ (V-PDB) (Camuera *et al.*, 2014), even in consideration of a diffuse emission of pure mantellic sources of CO_2 (-4.0‰ to -6.4‰; Kyser, 1986; Deines, 2002), which would account for $\delta^{13}C$ for the carbonates between -3.0 and -5.4‰ (V-PDB). Contribution of aeolian marine carbonates show less negative signatures (around 0‰). Consequently, the relatively negative $\delta^{13}C$ values of the dolomite of this study discard other non-pedogenic hypotheses for the origin of these carbonates.

The $\delta^{18}O$ values range from -2.85 to +0.91‰ (V-PDB), with more negative values corresponding to calcite and less negative ones to dolomite (Table S2 and Fig. 7B). The precipitation of dolomite occurs in equilibrium with meteoric waters having $\delta^{18}O$ values of around -3‰ (V-SMOW), *i.e.* close to present local meteoric water (-3.5 to -4‰ *vs.* V-SMOW; Figs. 14 and 15). Meteoric waters with $\delta^{18}O_{water}$ around +0.5‰ were determined in the case of calcite. These values indicate that calcite precipitated from highly evaporated water at most surficial levels in relation to multiple cyclic dissolution-evaporation/precipitation processes. On the other hand, the formation of dolomite took place in equilibrium with deeper meteoric waters (wetter zone). The rain waters percolate through the soil, and can be partially retained by abrupt changes in

permeability (alteration of volcanic rock, located mainly in the boundary between carbonates and basalt) in a space of a few metres deep. The occurrence of permanent non-circulating (fossil) water in the subsoil explains the more negative $\delta^{18}O$ calculated for meteoric water in equilibrium with dolomite for environmental temperatures compared to that calculated for calcite (Figs. 14 and 15). The calculated values agree with those of present and past rainwater and groundwater (-4.3‰ and -2.2‰, respectively; Gasparini *et al.*, 1990; Yanes *et al.*, 2011a,b). This is also consistent with the fact that the main commercial mineral-water spring of the island has a $\delta^{18}O$ of -3.7‰ (V-SMOW). Relatively homogenous $\delta^{18}O$ and $\delta^{13}C$ values of deeper levels indicate the dolomite formation in relation to the subsoil, an environment containing a greater amount of groundwater than soil *s. str.* (vadose or unsaturated zone). The disappearance of calcite at intermediate-deeper levels (around 1.5m) and the massive formation of dolomite below suggest different hydrodynamics of the soil media during the formation of each of these minerals. The specific hydrodynamics and transport properties in the subsoil also need to take into account those deduced from the study of the kinetics of geochemical processes involved in the formation of dolomite in soils.

4.4. Dolomite formation and maturation

This section deals with the formation of dolomite in depth and its relation to the surficial calcite. A plausible scenario suggests that calcite precipitation preceded the formation of dolomite in Mg-rich soils, so that dolomitization processes transported the isotopic signal associated with the biological activity of the more surficial layers of the caliche soil to deeper layers (Diaz-Hernandez *et al.*, 2013). According to this mechanism, the dolomite would not have formed directly from solution (primary

dolomite) but later through secondary replacement of previously precipitated calcite favoured by the presence of clay minerals (smectites).

The formation of the calcite of the upper levels (Bkkm1 horizon) and of the intermediate levels, where it coexists with dolomite, resulted from a major supply of exogenous Ca together CO_2, through Reaction 2. These inputs of Ca into the system also explain the formation of dolomite in Ca-deficient environment typical of incipient altered material (in this study represented by sample PL).

The calcite of the profile near the soil surface (Bkkm1 horizon) formed from direct precipitation into the spaces between the grains from percolating surficial solutions rich in Ca and the CO_2 resulting from root respiration in soil. This agrees with more negative $\delta^{13}C$ and $\delta^{18}O$ values measured for the calcite compared with those of dolomite (Fig. 7).

In addition to direct precipitation, calcite may be formed by reaction of dolomite with the silica to produce the sepiolite of the matrix and magnesian-rich calcite and calcite in core concretions observed at the intermediate levels of the profile (Fig. 10C-D), through the following reaction:

$$8CaMg(CO_3)_2 + 12SiO_2 + 2H_2O + 8Ca^{2+} \rightarrow Si_{12}O_{30}(OH)_4Mg_8 + 16CaCO_3 \quad (3)$$

As opposed to calcite, which precipitated later mostly from the soil solutions that infiltrated the surface levels of the soils (capillary groundwaters), dolomite precipitated firstly within a confined porous medium involving diffusion of reactants through a fluid fill composed of water adsorbed onto the surface of the clay-particles constituting the matrix. Water adsorbed onto clays in the subsoil reduces the bulk flow of the grain-boundary fluid or advective transport by infiltration. Under this diffusive regime, typical of viscous porous media, minerals precipitate at relatively high supersaturation

(Henisch, 1989). Thus, dolomite mesocrystals grew by adhesion of small crystal seeds or nanocrystalline units instead of deposition of ions onto the surface crystal (Fig. 8C). This type of crystal growth appears to favour the formation of poorly crystalline calcian dolomite instead of dolomite in the experimental precipitation (diffusion-controlled growth) of the Ca-Mg carbonate (Sanchez-Navas *et al.*, 2009). As indicated above, poorly crystalline calcian dolomite precipitated within a silicate-rich amorphous material that was probably the precursor of sepiolite and palygorskite, as suggested by the textures (*e.g.* Fig. 8). The sequence in the morphologies and the other crystal-growth features observed for dolomite throughout the study profile agrees with the early precipitation of a less mature calcian dolomite that later improved crystallinity and increased nanoparticle size (together with the size of coherent domains), cation ordering, and Mg content (Figs. 4D-F, 5A and Table 1). A poorly crystalline and calcian-rich dolomite evolved towards a more stoichiometric and crystalline dolomite via an Ostwald-ripening mechanism, as indicated by the X_{Mg} distribution (correlating with size distribution) curves exhibiting an asymmetric shape, with a tail towards the low-Mg (small crystallite size) side (Table 2A). This also agrees with the laboratory results on protodolomite-dolomite experimental transformation (Malone *et al.*, 1996; Kelleher and Redfern, 2002).

4.5. Weathering of volcanic deposits as potential geological sink for carbon

The soil profile studied resulted from the superposition of diverse physicochemical processes occurring under variable environmental conditions during the weathering of the volcanic deposits. The complex sequence of horizons indicates that the profile resulted from more than one soil-forming event, leading us to consider the soil as polycyclic, for which its uppermost level can be classified as Typic

Petrocalcid (Soil Survey Staff, 2014) or Petric Calcisol (IUSS-WRB, 2007). The occurrence of the Bt lenses in the Bkkm2 horizon (Fig. 2A and C) implies the prevalence of a humid climate, during which tephra was altered to clays and iron oxyhydroxides without significant carbonate precipitation. Minor carbonate precipitation could have occurred during this humid stage, but below the Bt lenses, at deeper levels where dolomite became supersaturated (dolomite of the Bkkm3 horizon; Fig. 2D). Later, environmental conditions evolved towards an arid-semiarid climate during which the uppermost massive caliche (Bkkm1; Fig. 2A-B) formed. On the other hand, the formation of less-carbonated levels could be the result of partial decalcification of previous caliches (here represented by the Bkkm3 horizon) under warm temperatures and higher soil moisture.

SOC and SIC stocks (expressed in mass per unit area, kg m^{-2}) have been computed for the individual soil layers, Ap horizons and 15 layers (Table 3A), as follows (Buell and Markewich, 2004; Soil Survey Staff, 2011):

$$SCSm = \rho b * 10 * d * (SC/100) * Cm \quad (4)$$

where:

SCSm = soil carbon storage (mass, in kilograms per square metre, kg/m^2) (total matrix, soil carbon)

ρb = soil bulk density, in grams per cubic centimetre (g/cm^3)

10 = factor for conversion from g/cm^3 to kg/m^2

d = depth of soil layer/horizon, in centimetres

SC = soil carbon concentration (organic or inorganic), in weight percentage

Cm = fraction of the profile volume occupied by soil (1 for these caliche soil layers and 0.74 for the Ap layer)

Inset B in Table 3 was constructed from SIC and SOC of the 16 caliche soil layers of Table 3A to emphasize soil carbon stocks (expressed in percentages) in the calcretes (Ap-Bkkm1, 0-1 m deep) and in the entire profile (mainly dolocretes). In the dolomitic soils studied, the accumulated atmospheric C stored as inorganic carbon reaches 586.1 kg m^{-2} (Table 3A).

The distribution of organic carbon with depth in the study profile describes the typical trend in soils with indurated horizons, with a high content in the horizon overlying the indurated caliche layers, and low quantities below (Fig. 3A; see also Diaz-Hernandez and Barahona, 2008).

The carbon of soils containing calcic and petrocalcic horizons typically include soil organic matter and inorganic carbon represented by calcite. This agrees with soil organic matter and the carbon stored in the calcite in the most surficial Ap-Bkkm1 horizon (1m deep), which reaches 3.5 and 110.4 kg m^{-2}, respectively (Table 3A). However, carbon bound as dolomite, when expressed in percentages, constitutes a 68.5% of the carbon stored in the overall soil profile (Table 3B) and, therefore, processes occurring in the subsoil should be taken into account in the carbon soil balances.

The estimation of aboveground biomass (AGB) is an essential aspect of studies of carbon stocks and global carbon balances (Ketterings *et al.*, 2001). Most AGB from forest ecosystem ranges between 25 and 70 kg m^{-2} (*e.g.* Muller, 1982; Rana *et al.*, 1988; Shrestha *et al.*, 2000). The soil organic carbon in tropical peats varies between 50 and 350 kg m^{-2}, with an average of 110 kg m^{-2} (Page *et al.*, 2011; Farmer *et al.*, 2014). On the other hand, arid climate areas present a very low accumulation of organic carbon. Nevertheless, this study demonstrates that, under this climate regime, the carbon is

stored mainly as inorganic carbon in the soil (pedogenic calcite) and subsoil (pedogenic dolomite) derived from volcanic substrates.

5. CONCLUDING REMARKS

The weathering of volcanic rocks can play an important role in the fixation of atmospheric CO_2, as deduced from the study case, where an unusually thick caliche soil (mainly dolomitic) formed on a basaltic substrate. It is proposed that, during the first stages of hydrous alteration of the glass and silicates of the volcanic tephra, clay minerals and related amorphous materials played an important kinetic role in the dolomite formation from basalts. Geochemical and mineralogical zoning observed throughout the profile indicates that the complex sequence of horizons observed in the soil studied resulted from the superposition of diverse physicochemical processes occurring under variable environmental conditions during the weathering of volcanic deposits (polycyclic soils).

The isotopic fractionation observed in the pedogenic carbonates throughout the profile derived from the infiltration of CO_2-rich soil waters with a clear biogenic signature. The dolomite precipitated in equilibrium with meteoric waters in the subsoil, whereas the calcite precipitated from evaporated water near to the surface. More surficial calcite caliches result from multiple cyclic dissolution-evaporation/precipitation processes under arid/semiarid environment. On the other hand, deeper dolomite precipitated in equilibrium with water in the deeper zone of the soil. The precipitation of dolomite took place first, before that of calcite, from bottom to top in the soil profile, and occurred within a clay-rich matrix. The presence of clay minerals favoured the existence of an almost permanent water-saturated zone in the arid/semiarid

environment. It is also responsible of the formation of dolomite, which matures with depth due to the increase of Mg/Ca close to the basalt substrate.

The concentration of CO_2 in the soil proved to be two orders of magnitude higher than in the atmosphere. This study clearly evidences that chemical weathering of basaltic rocks consumes this pedogenic CO_2 which precipitates as dolomite in the soils.

ACKNOWLEDGEMENTS

This work was financed by the research project P11-RNM-7067 (Junta de Andalucía, Spain) and is a contribution of the research group RNM-179 of the Junta de Andalucía. We would like to thank A. González, M. M. Abad, C. Hernández, M. A. Hidalgo, O. Cazalla, I. Moreno and J. Montes (C.I.C. and Department of Mineralogy, University of Granada), and E. J. Porcel (IFAPA) for the guidance with the analytical studies and sample preparation. David Nesbitt revised the English version of the manuscript.
We also wish to thank Oliver A. Chadwick and other anonymous reviewers, Associate Editor Dan Sinclair, and Executive Journal Editor Marc Norman for very thorough reviews and helpful comments on the manuscript.

References

Al-Aasm I. S., Taylor B. E. and South B. (1990) Stable isotope analysis of multiple carbonate samples using selective acid extraction. Chem. Geol. **80**, 119-125

Alonso-Zarza A. M., Bustamante L., Huerta P., Rodríguez-Berriguete A. and Huertas M. J. (2016) Chabazite and dolomite formation in a dolocrete profile: An example of a complex alkaline paragenesis in Lanzarote, Canary Islands. Sediment. Geol. **337**, 1-11.

Anderson S. P., Dietrich W. E. and Brimhall G. H. (2002) Weathering profiles, mass balance analysis, and rates of solute loss: linkages between weathering and erosion in a small, steep catchment. Geol. Soc. Am. Bull. **114**, 1143-1158.

Arvidson R. S. and Mackenzie J. A. (1999) The dolomite problem: control of precipitation kinetics by temperature and saturation state. Am. J. Sci. **299**, 257-288.

Balcells R., Barrera J. L., Gómez Saínz J. A., Hernán F., Schmincke H., Merlos A., Ruíz M., Brändle J., Meco J. and Vidal Romaní J. R. (1992) Mapa Geológico de España 1:100.000, hoja nº 21-22 (Gran Canaria). IGME.

Bender M. M., Rouhani I., Vines H. M. and Black C. C. (1973) $^{13}C/^{12}C$ ratio changes in crassulaceam acid metabolism plants. Plant Physiol **52**, 427-430.

Bern C. R., Thompson A. and Chadwick O. A. (2015) Quantification of colloidal and aqueous element transfer in soils: the dual-phase mass balance model. Geochim. Cosmochim. Acta **151**, 1-18.

Bramwell D. (1997) Flora of the Canary Islands: Pocket Guide. Ed. Rueda S. L., Madrid.

Buell G. R. and Markewich H. W. (2004) Data compilation, synthesis, and calculations used for organic-carbon storage and inventory estimates for mineral soils of the Mississippi River Basin. USGS Professional Paper 1686-A. Madison, WI: U.S. Geological Survey. http://pubs.er.usgs.gov/publication/pp1686A

Cabrera M. C. and Custodio E. (2004) Groundwater flow in a volcanic-sedimentary coastal aquifer: Telde area, Gran Canaria, Canary Islands, Spain. Hydrogeology J. **12**, 305-320.

Caldeira K. and Rau G. H. (2000) Accelerating carbonate dissolution to sequester carbon dioxide in the ocean, geochemical implications. Geophys. Res. Lett. **27**, 225-228.

Camuera J., Alonso-Zarza A.M., Rodríguez-Berriguete A. and Rodriguez-Gonzalez A. (2014) Origin and palaeo-environmental significance of the Berrazales carbonate spring deposit, North of Gran Canaria Island, Spain. Sedimentary Geology **308**, 32-43.

Capo R. C., Whipkey C. E., Blachère J. R. and Chadwick O. A. (2000) Pedogenic origin of dolomite in a basaltic weathering profile, Kohala peninsula, Hawaii. Geology **28**, 271-274.

Carracedo J. C., Pérez-Torrado F. J., Ancoechea E., Meco J., Hernán F., Cubas C. R., Casillas R., Rodríguez-Badiola E. and Ahijado A. (2002) Cenozoic vulcanism II: the Canary Islands. In: The Geology of Spain (F.A.W. Gibbons, T. Moreno, Eds.). Geological Society of London, 438-472.

Cerling T. E. (1984) The stable isotopic composition of modern soil carbonates and its relationships to climate. Earth Planet. Sc. Lett. **71**, 229-240.

Cerling T. E. (1991) Carbon dioxide in the atmosphere: evidence from cenozoic and mesozoic paleosols. Am. J. Sci. **291**, 377-400.

Cerling T. E. and Hay R. L. (1986) An isotopic study of paleosol carbonates from Olduvai Gorge. Quaternary Res. **25**, 63-78.

Cuadros J., Diaz-Hernandez J. L., Sanchez-Navas A., Garcia-Casco A. and Yepes J. (2016) Chemical and textural controls on 1 the formation of sepiolite, palygorskite and dolomite in volcanic soils. Geoderma **271**, 99-114.

Deelman J. C. (2011) Low-Temperature Formation of Dolomite and Magnesite (version 2.3) Geology Series Compact Disc Publication, Eindhoven, The Netherlands. http:/www.jcdeelman.demon.nl/dolomite/bookprospectus.html

Deines P. (1980) The isotopic composition of reduced carbon. In: Fritz, A., Fontes, P. (Eds.). The Terrestrial Environment. Handbook of Environmental Isotope Geochemistry. Elsevier Scientific Press, p. 329-434.

Deines P. (2002) The carbon isotope geochemistry of mantle xenoliths. Earth-Science Reviews **58**, 247-278.

Diaz-Hernandez J. L. and Barahona E. (2008) The effect of petrocalcic horizons on the content and distribution of organic carbon in a Mediterranean semiarid landscape. Catena **74**, 80-86.

Diaz-Hernandez J. L. (2010) Is soil carbon storage underestimated? Chemosphere **80**, 346-349.

Diaz-Hernandez J. L., Sanchez-Navas A. and Reyes E. (2013) Isotopic evidence for dolomite formation in soils. Chem. Geol. **347**, 20-33.

Dodd M. S., Papineau D., Grenne T., Slack J. F., Rittner M., Pirajno F., O'Neil J. and Little C. T. S. (2017) Evidence for early life in Earth's oldest hydrothermal vent precipitates. Nature **543**, 60-64.

Emrich K., Ehhalt D. H. and Vogel J. C. (1970) Carbon isotope fractionation during the precipitation of calcium carbonate. Earth Planet. Sc. Lett. **8**, 363-371.

Falkowski P. G., Scholes R. J., Boyle E., Canadell J., Canfield D., Elser J., Gruber N., Hibbard K., Högberg P., Linder S., Mackenzie F. T., Moore III B., Pedersen T., Rosenthal Y., Seitzinger S., Smetacek V. and Steffen W. (2000) The Global Carbon Cycle: a test of our knowledge of Earth as a System. Science **290** (5490), 291-96.

Farmer J., Matthews R., Smith P., Langan C., Hergoualc'h K., Verchot L. and Smith J. O. (2014) Comparison of methods for quantifying soil carbon in tropical peats. Geoderma 214-215, 177-183.

Friedli H., Lotscher H., Oeschger H., Siegenthaler U. and Stauffer B. (1986) Ice core record of the $^{13}C/^{12}C$ ratio of atmospheric CO_2 in the past two centuries. Nature **324**, 237-238.

Friedman I. and O'Neil J. R. (1977) Compilation of stable isotope fractionation factors of geochemical interest. In: M. Fleischer (Ed.), Data of Geochemistry. U. S. Geol. Surv. Prof. Pap. 440-KK, 1-12.

García B., Beaumont V., Perfetti E., Rouchon V., Blanchet D., Oger P., Dromart G., Huc A.-Y. and Haeseler F. (2010) Experiments and geochemical modelling of CO_2 sequestration by olivine: potential, quantification. Appl. Geochem. **25**, 1383-1396.

Garcia-Casco A. (2007) Magmatic paragonite in trondhjemites from the Sierra del Convento mélange, Cuba. Am. Mineral. **92**, 1232-1237.

Gasparini A., Custodio E., Fontes J. Ch., Jimenez J. and Nuñez J. A. (1990) A geochemical and isotopic study of groundwater flow paths in a volcanic area under semi-arid climatic conditions (Amurga, Gran Canaria, Canary Islands). J. Hydrology **114**, 61-91.

Gislason S. R., Wolff-Boesnisch D., Stefánsson A., Oelkers E. H., Gunnlaugsson E., Sigurdardottir H., Sigfusson B., Broecker W. S., Matter J. M., Stute M., Axelsson G. and Fridriksson T. (2010) Mineral sequestration of carbon dioxide in basalt: A pre-injection overview of the CarbFix project. Int. J. Greenh. Gas Control **4**, 537-545.

Goff F. and Lackner K. S. (1998) Carbon dioxide sequestering using ultramafic rocks. Environ. Geosc. **5**, 89-101.

Goldsmith J. R. and Graf D. L. (1958) Structural and compositional variations in some natural dolomites. J. Geol. **66**, 678-693.

Guillou H., Pérez-Torrado, F. J., Hansen-Machín, A. R., Carracedo, J. C. and Gimeno D. (2004) The Plio-Quaternary volcanism evolution of Gran Canaria based on new K-Ar ages and magnetoestratigraphy. J. Volcanol. Geotherm. Res. **135**, 221-246.

Gysi A. P. and Stefánsson A. (2011) CO_2-water-basalt interaction. Numerical simulation of low temperature CO_2 sequestration into basalts. Geochim. Cosmochim. Acta **75**, 4728-4751.

Gysi A. P. and Stefánsson A. (2012) CO_2-water-basalt interaction. Low temperature experiments and implications for CO_2 sequestration into basalts. Geochim. Cosmochim. Acta **81**, 129-152.

Henisch H. K. (1989) Crystals in gels and Liesegang rings. Cambridge University Press, Cambridge, p. 197.

Houghton, R.A. (2007) Balancing the Global Carbon Budget. Ann. Rev. Earth Pl. Sc. **35**, 313-347.

Huerta P., Rodríguez-Berriguete A., Martín-García R., Martín-Pérez A., La Iglesia A. and Alonso-Zarza A. M. (2015) The role of climate and eolian dust input in calcrete formation in volcanic islands (Lanzarote and Fuerteventura, Spain). Palaeogeography, Palaeoclimatology, Palaeoecology **417**, 66-79.

Irwin H., Curtis C. D. and Coleman M. (1977) Isotopic evidence for source of diagenetic carbonates formed during burial of organic-rich sediments. Nature **269**, 209-213.

ITGE (1990) Memoria y mapa geológico a escala 1:100.000 de la Isla de Gran Canaria. [Geologic map and guidebook of Gran Canaria Island at 1:100.000 scale]. Instituto Tecnológico Geominero de España, Madrid.

IUSS Working Group WRB (2007) World Reference Base for Soil Resources 2006, first update. World Soil Resources Reports, n^{er} 103. Rome: FAO.

Kaczmarek S. E. and Sibley D. F. (2011) On the evolution of dolomite stoichiometry and cation order during high-temperature synthesis experiments: an alternative model for the geochemical evolution of natural dolomites. Sediment. Geol. **240**, 30-40.

Kelleher I. J. and Redfern S. A. T (2002) Hydrous calcium magnesium carbonate, a possible precursor to the formation of sedimentary dolomite. Mol. Simul. **28**, 557-572.

Ketterings Q. M., Coe R., van Noordwijk M., Ambagau Y. and Palm C. A. (2001) Reducing uncertainty in the use of allometric biomass equations for predicting above-ground tree biomass in mixed secondary forests. For. Ecol. Manag. **146**, 199-209.

Kim S. T. and O'Neil J. R. (1997) Equilibrium and nonequilibrium oxygen isotope effects in synthetic carbonates. Geochim. Cosmochim. Acta **61**, 3461-3475.

Krauskopf K. B. and Bird D. K. (1995) Introduction to Geochemistry. Second ed., McGraw-Hill, New York, p. 647.

Kyser T. K. (1986) Stable isotope variations in the mantle. Reviews in Mineralogy and Geochemistry **16**, 141-164.

Lackner K. S. (2002) Carbonate chemistry for sequestration fossil carbon. Annu. Rev. Energy Environ. **27**, 193-232.

Lal R. (2008a) Carbon sequestration. Phil. Trans. R. Soc. B **363**, doi: 10.1098/rstb.2007.2185.

Lal R. (2008b) Sequestration of atmospheric CO_2 in global carbon pools. Energy Environ. Sci. **1**, 86-100.

Land L. S. (1992) The dolomite problem: stable and radiogenic isotope clues. In: Clauer, N. and Chaudhary, S. (Eds.), Isotopic signatures of sedimentary records. Lect. Notes Earth Sci. **43**, pp. 49-68.

Land L. S. (1998) Failure to precipitate dolomite at 25°C from dilute solutions despite 1000-fold oversaturation after 32 years. Aquat. Geochem. **4**, 361-368.

Loeppert R. H. and Suárez D. L. (1996) Carbonate and gypsum. In: Sparks, D. L. (Ed.), Methods of Soil Analysis, Part 3 Chemical Analysis. SSSA Book series, No 5. ASA & SSSA, Madison, WI, pp. 437-474.

Lorimer G. W. and Cliff G. (1976) Analytical electron microscopy of minerals. In: Wenk, H.R. (Ed.), Electron Microscopy in Mineralogy. Springer-Verlag, Berlin, pp. 506-519.

Malone J. M., Baker P. A. and Burns S. J. (1996) Recrystallization of dolomite: An experimental study from 50-200°C. Geochim. Cosmochim. Acta **60**, 2189-2207.

Mangas J., Menéndez I., Ortiz J. E. and Torres T. (2008) Coastal eolianites of upper Pleistocene in the "Sitio de interés científico de Tufia" (Gran Canaria Island): sedimentology, petrography and aminochronology. Geotemas **10**, 1405-1408.

Martín-Ramos J. D., Diaz-Hernandez J. L., Cambeses A., Scarrow J. H., López-Galindo A. (2012) Pathways for quantitative analysis by X-ray diffraction. In: Aydinalp, C. (Ed.), An Introduction to the Study of Mineralogy. InTech, Rijeka, Croatia, pp. 73-92.

McCrea J. M. (1950) On the isotopic chemistry of carbonates and a paleotemperature scale. J. Chem. Phys. **18**, 849-857.

McDougall I. and Schmincke H. U. (1976) Geochronology of Gran Canaria, Canary Islands: age of shield building volcanism and other magmatic phases. Bull. Volcanol. **40**, 1-21.

McGrail B. P., Schaef H. T., Ho A.M., Chien Y.-J., Dooley J. J. and Davidson C. L. (2006) Potential for carbon dioxide sequestration in flood basalts, J. Geophys. Res., **111**, B12201, doi:10.1029/2005JB004169.

Menéndez I., Diaz-Hernandez J. L., Mangas J., Alonso I. and Sánchez-Soto P. J. (2007) Airborne dust accumulation and soil development in the North-East sector of Gran Canaria (Canary Islands, Spain). J. Arid Environ. **71**, 57-81.

Mestre A. and Felipe L. (2012) Atlas climático de los archipiélagos de Canarias, Madeira y Azores. Temperatura del aire y precipitación (1971-2000). Lisboa, Agencia estatal de Meteorología e Instituto de Meteorología de Portugal, 80 pp.

Muller R. N. (1982) Vegetation pattern in the mixed mesophytic forest of eastern Kentucky. Ecology **63**, 1901-1917.

Olajire A. A. (2013) A review of mineral carbonation technology in sequestration of CO_2. J. Petrol. Sci. Eng. **109**, 364-392.

Page S. E., Rieley J. O. and Banks C. J. (2011) Global and regional importance of the tropical peatland carbon pool. Glob. Change Biol. **17**, 798-818, doi:10.1111/j.1365-2486.2010.02279.x.

Pate J. S. (2001) Carbon Isotope Discrimitation and Plant Water-Use Efficiency: Case Scenarios for C3 Plants. In "Stable Isotope Techniques in the Study of Biological Processes and Funtioning of Ecosystems" (Eds. M. Unkovich, J. Pate, A. McNeill, D.J. Gibbs) pp. 19-36. (Current Plant Science and Biothecnology in Agriculture).

Pérez-Torrado F. J., Carracedo J. C. and Mangas J. (1995) Geochronology and stratigraphy of the Roque Nublo Cycle, Gran Canaria, Canary Islands. J. Geol. Soc. London **152**, 807-818.

Quade J., Cerling T. E. and Bowman J. R. (1989) Systematic variations in the scale carbon and oxygen isotopic composition of pedogenic carbonate along elevation transect in the southern Great Basin, USA. Geol. Soc. Am. Bull. **101**, 467-475.

Quade J. and Cerling T. E. (1990) Stable Isotopic Evidence for a Pedogenic Origin of Carbonates in Trench 14 near Yucca Mountain, Nevada. Science **250**, 1549-1552.

Rana B. S., Singh S. P. and Singh R. P. (1988) Biomass and productivity of centralHimalayan Sal (Shorea robusta) forest. Trop. Ecol. **29**, 1-5.

Reeder R. J. and Sheppard C. E. (1984) Variation in lattice parameters in some sedimentary dolomites. Am. Miner. **69**, 520-527.

Reyes E., Pérez del Villar L., Delgado A., Cortecci G., Núñez R., Pelayo M. and Cózar J. (1998) Carbonatation processes at the El Berrocal analogue granitic system (Spain): mineralogical and isotopic study. Chem. Geol. **150**, 293-315.

Rodríguez M., Neris J., Tejedor M. and Jiménez C. (2010) Soil temperature regimes from different latitudes on a subtropical island (Tenerife, Spain). Soil Sci. Soc. Am. J. **74**, 1662-1669.

Romanek C. S., Grossman E. L. and Morse J. W. (1992) Carbon isotopic fractionation in syntetic aragonite and calcite: Effects of temperature and precipitation rate. Geochim. Cosmochim. Acta **56**, 419-430.

Rosenbaum J. and Sheppard S. M. F. (1986) An isotopic study of siderites, dolomites and ankerites at high temperatures. Geochim. Cosmochim. Acta **50**, 1147-1150.

Salomons W. and Mook W. G. (1976) Isotope geochemistry of carbonate dissolution and reprecipitation in soils. Soil Sci. **122**, 15-24.

Salomons W., Goudie A. and Mook W. G. (1977) Isotopic composition of calcrete deposits from Europe, Africa and India. Earth Surf. Proc. Land. **3**, 43-57.

Sánchez-Navas A., Martín-Algarra A., Rivadeneyra M. A., Melchor S. and Martín-Ramos J. D. (2009) Crystal-growth behaviour in Ca–Mg carbonate bacterial spherulites. Cryst. Growth Des. **9**, 2690-2699.

Shrestha R., Karmacharya S. B. and Jha P. K. (2000) Vegetation analysis of natural and degraded forests in Chitrepani in Siwalik region of Central Nepal. Trop. Ecol. **41**, 111-114.

Sigman D. M. and Boyle E. A. (2000) Glacial/interglacial variations in atmospheric carbon dioxide. Nature **407**, 859-869.

Soil Survey Staff (2011) Soil Survey Laboratory Information Manual. Soil Survey Investigations Report No. 45, Version 2.0. R. Burt (ed.). U.S. Department of Agriculture, Natural Resources Conservation Service.

Soil Survey Staff (2014) Keys to Soil Taxonomy. 12th ed., Washington: USDA-Natural Resources Conservation Service.

Thorseth I. H., Furnes H. and Tumyr O. (1991) A textural and chemical study of Icelandic palagonite of varied composition and its bearing on the mechanism of the glass-palagonite transformation. Geochim. et Cosmochim. Acta **55**, 731-749, doi:10.1016/0016-7037(91)90337-5.

Thorseth I. H., Furnes H. and Heldal M. (1992) The importance of microbiological activity in the alteration of natural basaltic glass. Geochim. Cosmochim. Acta **56**, 845-850 10.1016/0016-7037(92)90104-Q.

Thorseth I. H., Torsvik T., Furnes, H. and Muehlenbachs K. (1995) Microbes play an important role in the alteration of oceanic crust: Chem. Geol. **126**, 137-146, doi:10.1016/0009-2541(95)00114-8.

Urey H. C. (1952) The Planets, Their Origin and Development. Yale University Press, New Haven, Conn., p.135.

USDA-NRCS (2004) Soil Survey Laboratory Methods Manual, Soil Survey Investigations Report No. 42, Version 4.0, 700 pp.

Usdowski E. and Hoefs J. (1993) Oxygen isotope exchange between carbonic acid, bicarbonate, carbonate, and water: a re-examination of the data of McCrea (1950) and an expression for the overall partitioning of oxygen isotopes between the carbonate species and water. Geochim. Cosmochim. Acta **57**, 3815-3818.

Van Tuyl F. M. (1916) The present status of the dolomite problem. Science **44**, 688-690.

Vihermaa L. E., Waldron S., Domingues T., Grace J., Cosio E. G., Limonchi F., Hopkinson C., da Rocha H. R. and Gloor E. (2016) Fluvial carbon export from a lowland Amazonian rainforest in relation to atmospheric fluxes. J Geophys. Res.-Biogeosciences **121**, 3001-3018.

Whipkey C. E., Capo R. C., Hsieh J. C. C. and Chadwick O. A. (2002) Development of magnesian calcite and dolomite in Quaternary soils on the island of Hawaii. J. Sed. Res. **72**, 158-165.

Whitney D. L. and Evans B. W. (2010) Abbreviations for names of rock-forming minerals. Am. Mineral. **95**, 185-187.

Wu J. C. S., Sheen J.-D., Chen S. Y. and Fan Y.-C. (2001) Feasibility of CO_2 fixation via artificial rock weathering. Ind. Eng. Chem. Res. **40**(18), 3902-3905.

Yanes Y., Delgado A., Castillo C., Alonso M. R., Ibañez M., De la Nuez J. and Kowalewski M. (2008) Stable isotope $\delta^{18}O$, $\delta^{13}C$ and δD signatures of recent terrestrial communities from a low-latitude, oceanic setting: Endemic land snails, plants, rain, and carbonate sediments from the eastern Canary Islands. Chem. Geol. **249**, 377-392.

Yanes, Y., Aguirre, J., Alonso, M. R., Ibañez, M. and Delgado, A. (2011a) Ecological fidelity of Pleistocene-Holocene land snail shell assemblages preserved in carbonate-rich paleosols. Palaios **26**, 406-419.

Yanes Y., Yapp C. J., Ibañez M., Alonso M. R., De-la-Nuez J., Quesada M. L., Castillo C. and Delgado A. (2011b) Pleistocene-Holocene environmental change in the Canary Archipelago as inferred from the stable isotope composition of land snail shells. Quaternary Res. **75**, 658-669.

FIGURE CAPTIONS

Fig. 1. A) Satellite image of the Gran Canaria evidencing a conical shape resulting from its volcanic origin. The island is composed of a central jagged volcanic mountain and surrounded by cliffs and bays. Two differentiated landscapes are appreciated: one with a more arid climate on the southern side and a more humid one on the north-eastern side of the island; the study area is located in the more southern part (inset). B) Geological cartography superposed to a Google Earth image of the eastern region of Gran Canaria, where sediments and the volcanic materials associated with the Roque-Nublo and Post-Roque-Nublo magmatic episodes are indicated (see also right-hand geological column). The study profile (El Goro) is located close to the bottom of slope of the Roque-Nublo volcano. C) Geological cross-section including the groundwater level corresponding to 1998 based on Cabrera and Custodio, 2004.

Fig. 2. A) General view of the pit outcrop showing the sampled profile (red line). In addition to the loose surficial horizon (Ap), three soil horizons can be established: Bkkm1, Bkkm2, and Bkkm3. B) Detail of the Bkkm1 horizon composed of a whitish caliche with traces of laminar structure. C) Massive caliche (Bkkm2) with red clayey lenses (Bt) including a fragment of volcanic tephra (Vt) and pinkish levels (PL), both corresponding to the altered volcanic material. D) Basal laminar caliche horizon (Bkkm3) over the basaltic substrate.

Fig. 3. XRD pattern sequence throughout the profile studied with an indication of the diverse horizons (number refers the depth in cm). The diffractograms are arranged from the top to down of the profile. Main XRD peaks corresponding to sepiolite,

palygorskite, quartz, low magnesian calcite, and calcian dolomite are indicated by arrows. Abbreviations (Whitney and Evans, 2010): Cal=calcite; Dol=dolomite; Felds=feldspars; Plg=palygorskite; Qz=quartz; Sep=sepiolite.

Fig. 4. Compositional, mineralogical, and crystallinity variations throughout the study profile with indication of the diverse horizons (number refers the depth in cm): A) Distribution of organic carbon. B) Carbonate distribution along the profile. C) Calcite and dolomite content (recalculated to 100). D) X_{Mg} content of dolomite determined from *a* lattice parameter ($X_{Mg}a$). E) Ratio of the intensity of (*015*) and (*110*) XRD peaks of dolomite along the profile. F) Full width of dolomite (*104*) peak at half its maximum intensity (FWHM).

Fig. 5. A) XRD diagrams of two representative samples of the study profile. The upper one from 60 cm depth corresponds to a low-magnesian calcite (X_{Mg}^{Cal} = 0.08) and a hardly evolved calcian dolomite (X_{Mg}^{Dol} = 0.42) of relatively poor crystallinity, evidenced by a high FWHM value (0.59º 2θ) for the (*104*) peak of the dolomite. No calcite appears in the lower diagram from the sample at 280 cm depth, which corresponds to a more ordered calcian dolomite (X_{Mg}^{Dol} = 0.48 and FWHM=0.23º 2θ). B) Grey-scale map drawn from the XRD patterns sequence of Fig. 4 (only the 24-46º 2θ interval is represented) with indication of the depth of the samples (y-axis). Shades of grey in the image correspond to the relative intensity of XRD peaks of calcite and dolomite. The main reflections of calcite (black) and dolomite (green) are indicated on the X-axis. The depth of the two XRD diagrams of Fig. 5A is also marked in the XRD map by dotted lines.

Fig. 6. Evolution of selected major and trace elements in soil profile, including the basaltic substrate (320 cm) from data of Table S1: A) Si, Ca, and Mg. B) Al and Fe. C) Na, K, and Ti. D) Heavy metals (V+Cr+Ni+Cu). E) Zirconium. F) Sum of rare-earth elements (REE). PL= Pinkish level corresponding to altered fragments of the volcanic tephra at 200 cm.

Fig. 7. A) $\delta^{13}C$ depth distribution of calcite (diamonds) and dolomite (squares) in the soil profile studied. B) $\delta^{18}O$ distribution of calcite and dolomite in the profile.

Fig. 8. SE images and EDX spectra from soil samples at 60 (A), 100 (B) and 300 (C and D) cm depth. A) Poorly crystalline calcian dolomite intergrown with fine-grained calcite and fibrous clays. B) Calcian dolomite rhombohedra tightly wrapped by sepiolite fibres. C) Isolated spherulite formed by the aggregation of calcian dolomite rhombohedra. D) A detail of C) showing idiomorphic calcian dolomite crystals but with irregular surfaces covered by very small fibres of palygorskite.

Fig. 9. A) TEM low-magnification image of calcian dolomite and sepiolite particles. EDX spectrum corresponds to the calcian dolomite rhombohedron. B) HAADF (high-angle annular dark-field) image of the previous rhombohedron exhibiting a patched contrast within. C) to D) X-ray maps of Si, Ca, and Mg, respectively. F) HRTEM lattice fringe image of an area close to the lower boundary (inset in A) of the rhombohedral crystal. Nanometre-sized coherent domains of the crystal are evidenced by the diverse orientations of the lattice fringes. G) SAED pattern of this area, where reciprocal distance 7.34 nm^{-1} corresponding to d*(006)* spacing (2.7 Å) is indicated (top left of Figure F). H) ELNES of C-*K*; Ca-$L_{2,3}$; O-*K* and Mg-*K* edges.

Fig. 10. A) Mineral-phase map of a sample at 60 cm depth. B) Si-Mg-Ca triangular diagram corresponding to the image A. The colour indicates the number of pixels with a specific chemical composition corresponding to sepiolite (Sep), dolomite (1), Ca-dolomite (2), Mg-calcite (3) and low-Mg calcite (4). C) and D) Insets of A) showing Mg X-ray (Kα) distribution maps of diverse carbonate concretions included in the sepiolite-rich matrix. An incipient dolomitized calcite concretion is shown in C. Arrows in Fig. D point to a calcite concretion partially transformed to sepiolite (I), and to dolomite (II); 1 and 2 correspond to dolomite and Ca-dolomite, 3 and 4 to Mg-calcite and calcite). Mg-riches areas correspond to the sepiolite of the matrix and of the rims of the concretions (white colour of the map).

Fig. 11. A) Mineral-phase map corresponding to a scarcely carbonated volcanic tephra (PL sample at 2m depth). Note the occurrence of dolomite in pores and vacuoles, smectite in the relics of the volcanic tephra and palygorskite plus sepiolite in the matrix. B) Corresponding Si-Mg-Ca triangular diagram showing the compositional fields of the diverse mineral phases.

Fig. 12. Determination of Si, Mg, and Ca gains in the soil profile through the calculation of the tau (τ) values representing the fractional mass gains (τ>0) relative to basalt parent material calculated as $\tau_{j,w} = \frac{C_{j,w} * C_{i,p}}{C_{j,p} * C_{i,w}} - 1$ (Anderson *et al.*, 2002, Bern *et al.*, 2015), C*j* and C*i* being the concentration in weight percentage of mobile elements *j* (Si, Mg, Ca) and of the selected immobile element *i* (Ti), respectively, and the subscripts *w* and *p* refer to weathered material).

Fig. 13. Theoretical isotope values of carbonates calculated from potential sources of carbon in the area (C3, CAM and C4 plants, and atmospheric CO_2). The green area corresponds to the most frequent range of C3 plants (–30‰ to –25‰; Deines, 1980) and the yellow area to the C4 range, whereas CAM plots in a middle range (Bender *et al.*, 1973; Pate, 2001). The pre-industrial atmospheric CO_2 has a $\delta^{13}C$ value of -6.5‰ (Friedli *et al.*, 1986) (-8‰ at present). The CO_2 in the soil is about 4.5‰ heavier than the plant biomass (Cerling, 1984, 1991). The isotopic difference between CO_2 and dissolved inorganic carbon (DIC) depends on the pH and temperature. This value is close to 0‰ at about pH 5, but is relatively independent of pH between 7.5 and 8 (Romanek *et al.*, 1992). For the isotopic theoretical calculation (DIC and carbonates) we considered a carbonate-bicarbonate enrichment of 1‰ (independent of the temperature) and the calcite-CO_2 equation described by Romanek *et al.* (1992) for temperatures of 15°C and 30°C (figure modified after Reyes *et al.*, 1998).

Fig. 14. Equilibrium temperature *vs.* $\delta^{18}O_{water}$ curves calculated from measured $\delta^{18}O_{carbonates}$ according to the equations of Kim and O'Neil (1997) and Irwin *et al.* (1977) for calcite (A) and dolomite (B). Blue rectangle corresponds to isotopic composition of the water in equilibrium with our natural carbonates. A narrow range of temperatures was considered (between 20 and 22ºC) because they are very homogeneous year round in the Canary Islands.

Fig. 15. Theoretical isotope composition calculated for the water in equilibrium with the precipitated calcite and dolomite along the study profile. Isotope composition of present meteoric water is also provided for comparison (blue rectangle).

TABLE CAPTIONS

Table 1. Unit-cell parameters, molar fraction of Mg (X_{Mg}), full width at half of the maximum (FWHM) of (*104*) and ratio of intensities of reflections (*015*) and (*110*) for Ca-dolomites throughout the studied profile.

Depth 0	a (Å)	c (Å)	V (Å^3)	XMg a	XMg c	XMg V	FWHM (º2θ)	$I_{(015)}/I_{(110)}$
-20	4.841	16.180	328.423	0.412	0.441	0.428	0.451	
-40	4.846	16.203	329.517	0.399	0.430	0.416	0.489	**0.26**
-60	4.838	16.203	328.449	0.420	0.430	0.427	0.586	
-80	4.837	16.151	327.302	0.422	0.455	0.439	0.331	**0.25**
-100	4.830	16.134	326.002	0.441	0.463	0.453	0.250	**0.35**
-120	4.835	16.150	326.931	0.429	0.455	0.443	0.316	**0.23**
-140	4.833	16.144	326.604	0.433	0.458	0.446	0.289	**0.29**
-160	4.830	16.146	326.212	0.442	0.457	0.451	0.237	**0.52**
-180	4.816	16.129	324.961	0.479	0.465	0.474	0.257	**0.41**
-200	4.817	16.162	324.743	0.477	0.449	0.466	0.255	**0.47**
-220	4.816	16.168	324.742	0.479	0.446	0.466	0.226	**0.45**
-240	4.819	16.141	324.660	0.470	0.459	0.467	0.236	**0.43**
-260	4.817	16.173	324.976	0.476	0.444	0.463	0.232	**0.40**
-280	4.817	16.138	324.263	0.477	0.461	0.471	0.237	**0.40**
-300	4.818	16.139	324.487	0.473	0.460	0.468	0.258	**0.42**

A

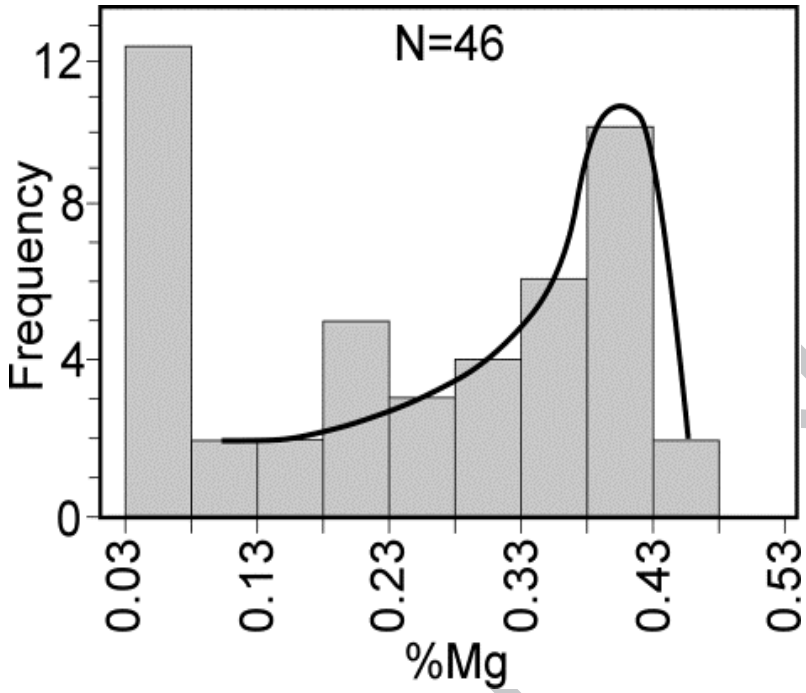

B

	Calcites				Dolomites			
	60 cm		160 cm		60 cm		160 cm	
	Mg	Ca	Mg	Ca	Mg	Ca	Mg	Ca
N	6		11		19		10	
Means	0.10	0.90	0.07	0.93	0.32	0.68	0.39	0.61
SD	0.03	0.03	0.06	0.05	0.08	0.08	0.03	0.03
min	0.06	0.85	0.03	0.83	0.19	0.55	0.34	0.55
max	0.15	0.94	0.19	0.97	0.45	0.81	0.45	0.66
median	0.09	0.91	0.05	0.95	0.32	0.68	0.40	0.60

A

	Depth cm	O.C. kg m^2	Inorganic Carbon Calcite kg m^2	Dolomite kg m^2
Ap	0	1.52	4.43	0.61
	-20	0.73	25.70	6.20
	-40	0.54	27.77	10.63
Bkkm1	-60	0.15	12.58	6.38
	-80	0.24	27.35	10.00
	-100	0.34	12.55	23.54
	-120	0.39	25.89	12.18
	-140	0.24	26.02	10.80
	-160	0.29	18.48	23.25
Bkkm2	-180	0.12	0.00	39.68
	-200	0.41	0.00	44.76
	-220	0.08	0.00	37.37
	-240	0.17	0.00	35.07
	-260	0.10	0.00	44.23
	-280	0.08	0.00	49.06
Bkkm3	-300	0.22	0.00	51.63
	Total	5.63	180.76	405.37

B

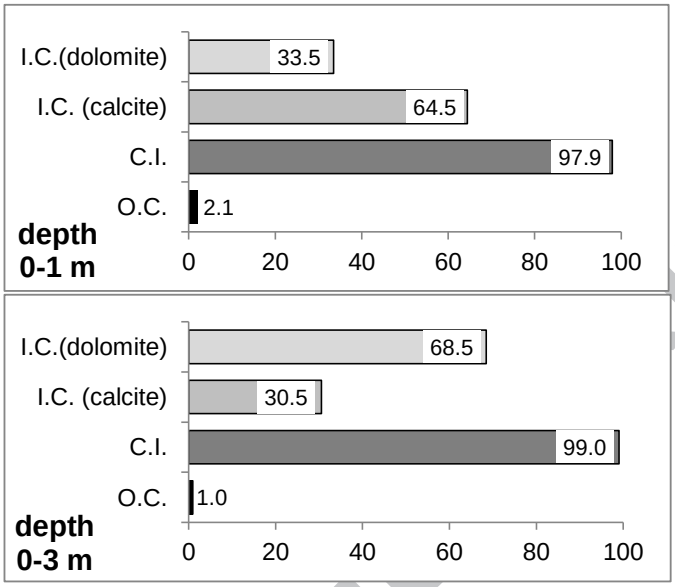

Figure 1

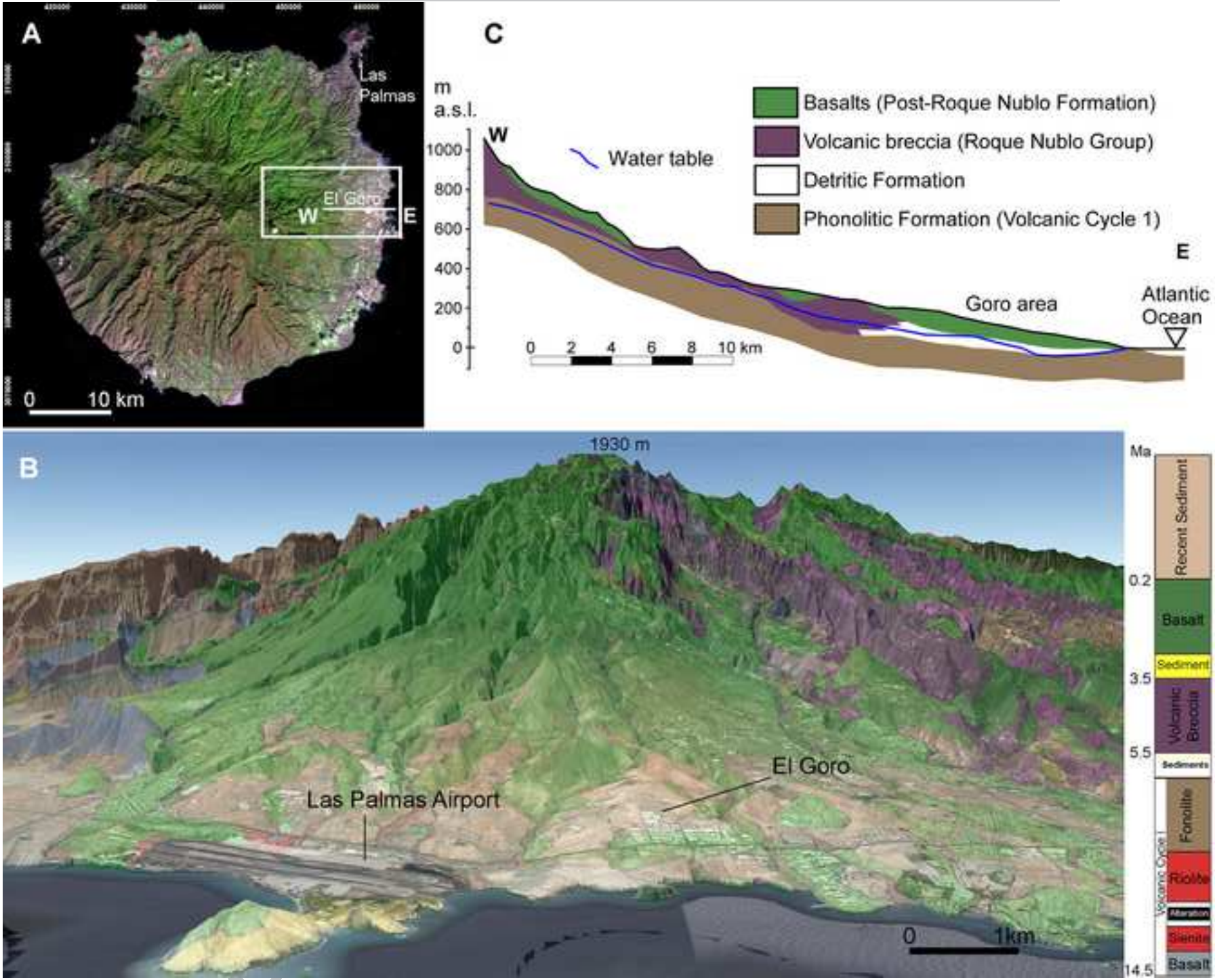

Figure 2

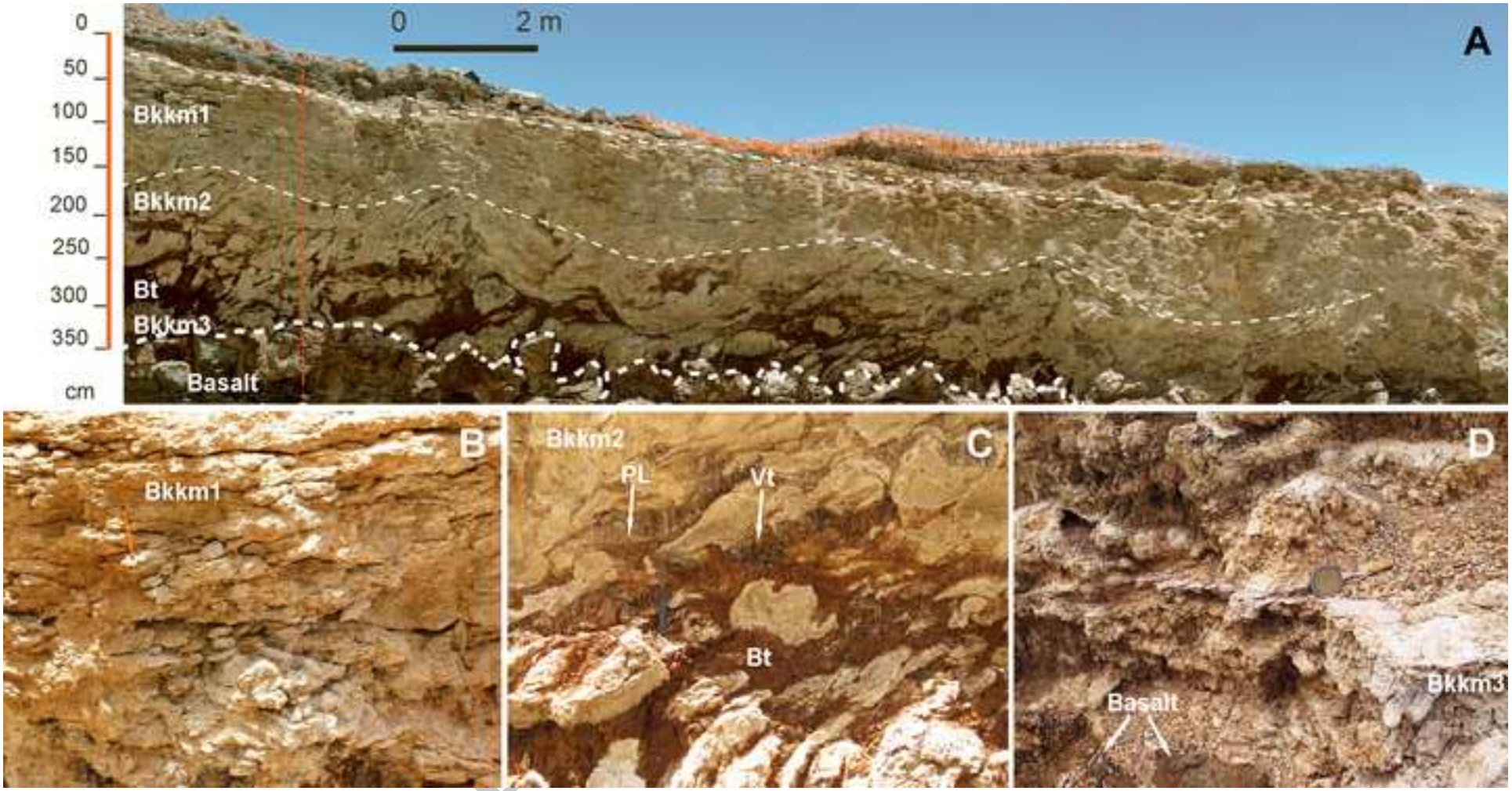

Figure 3

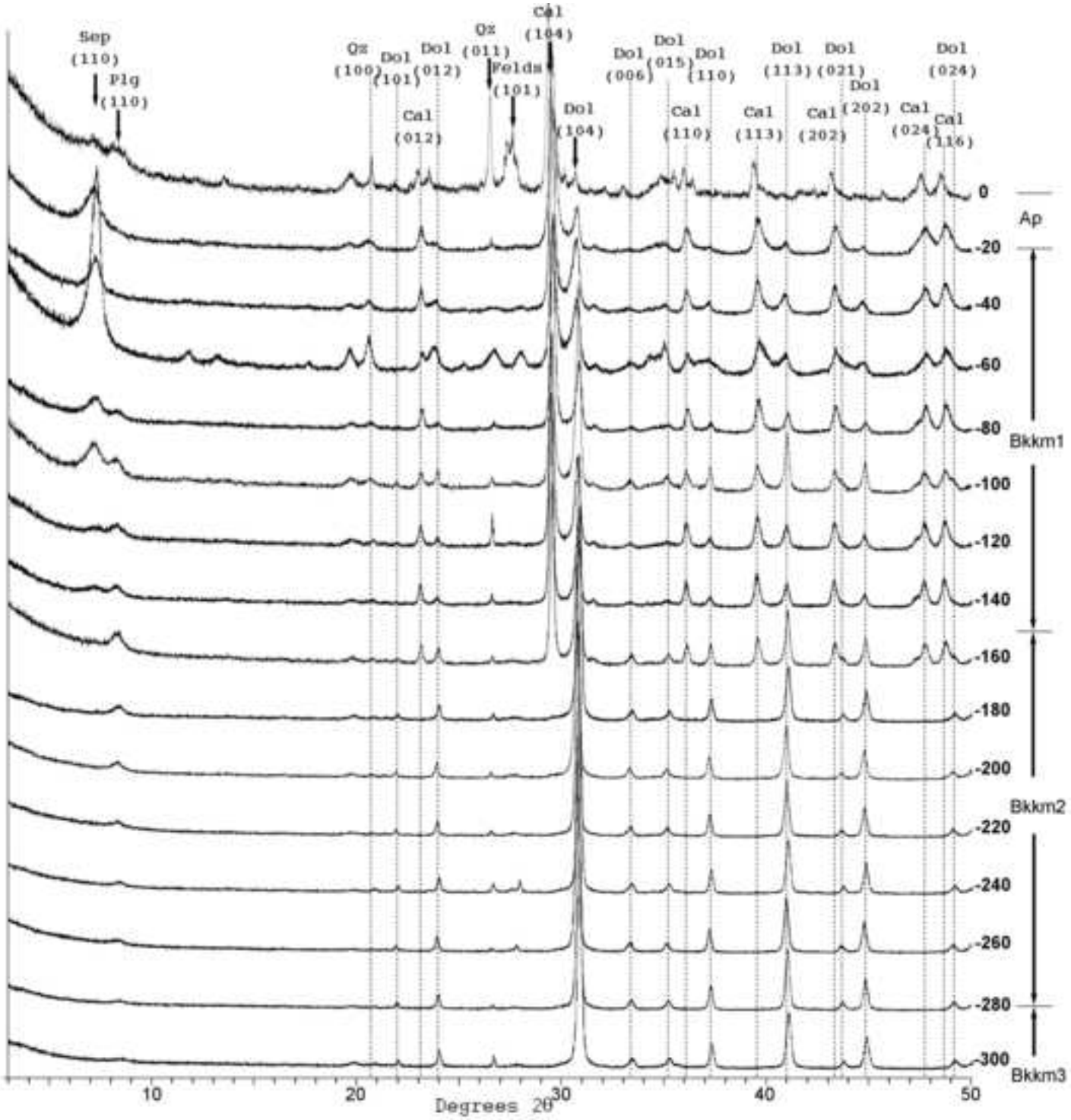

Figure 4

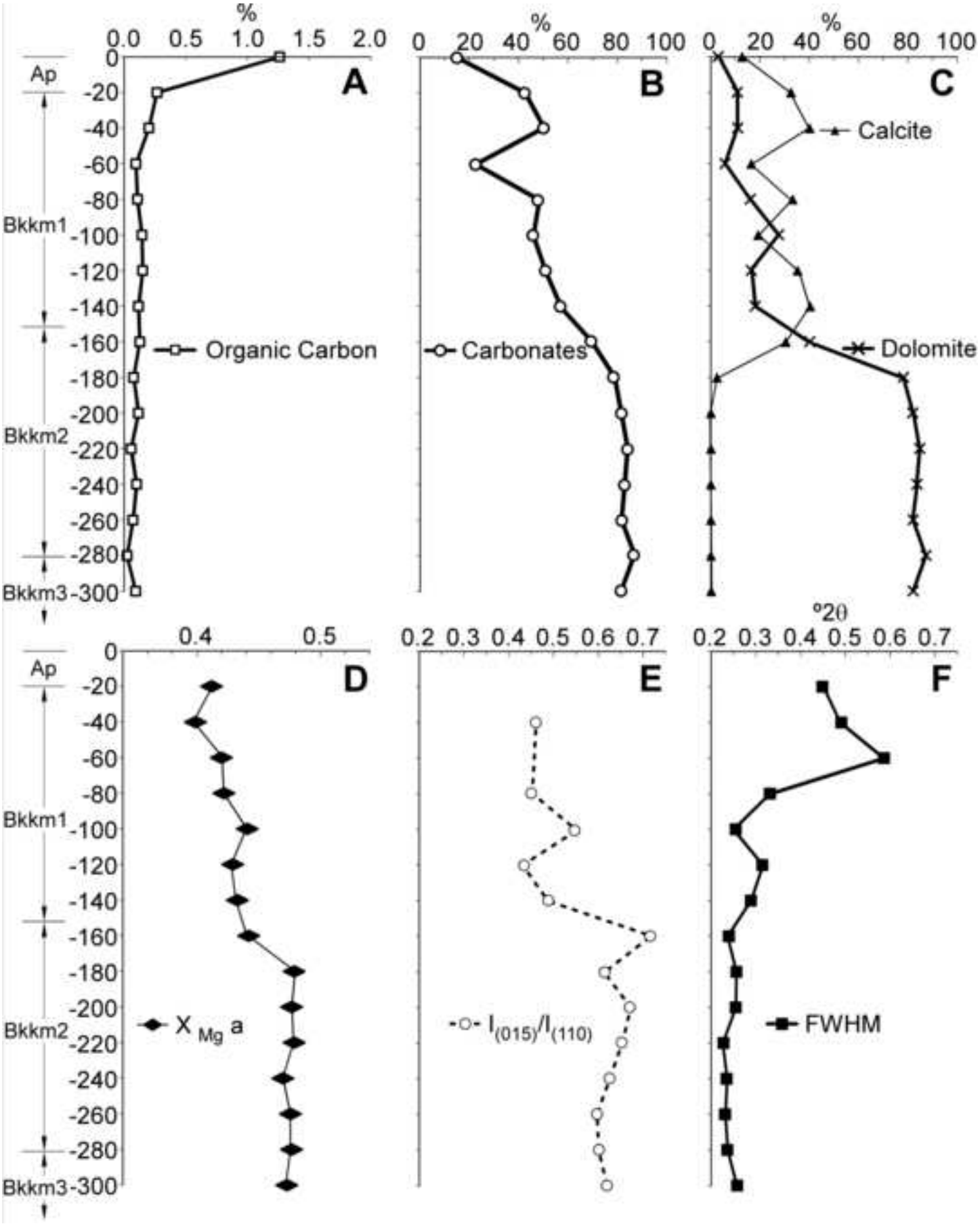

Figure 5

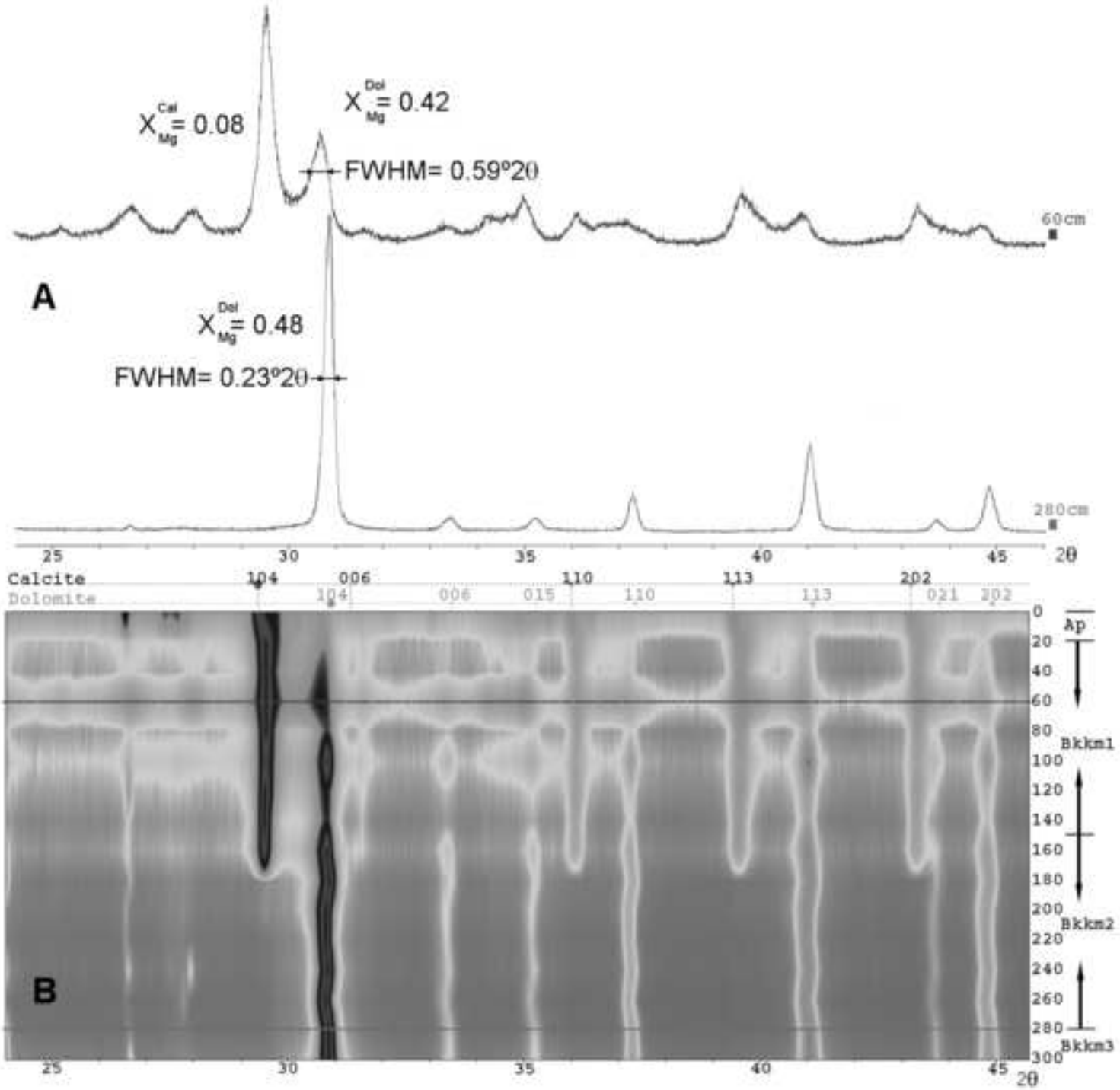

Figure 6

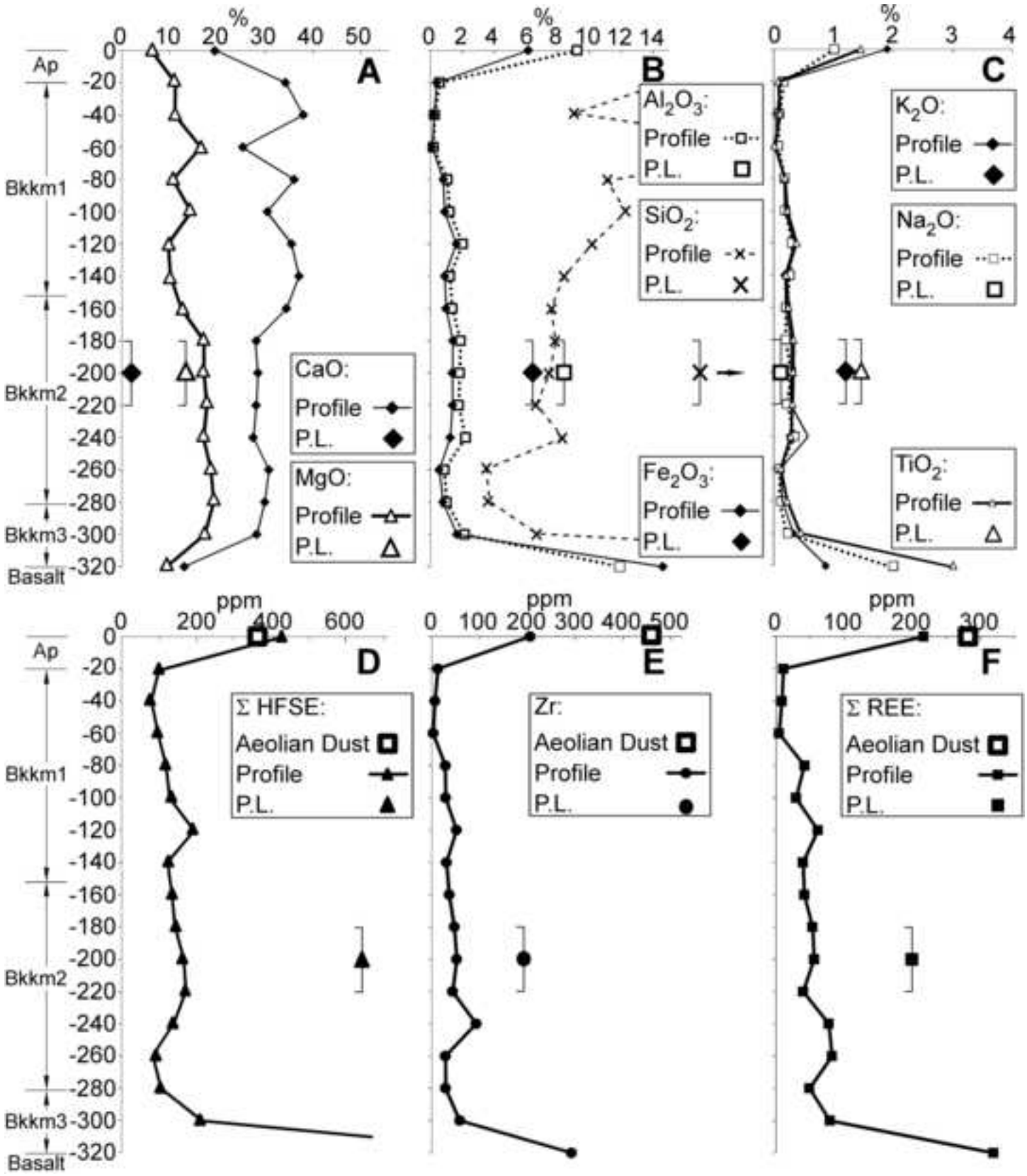

Figure 7

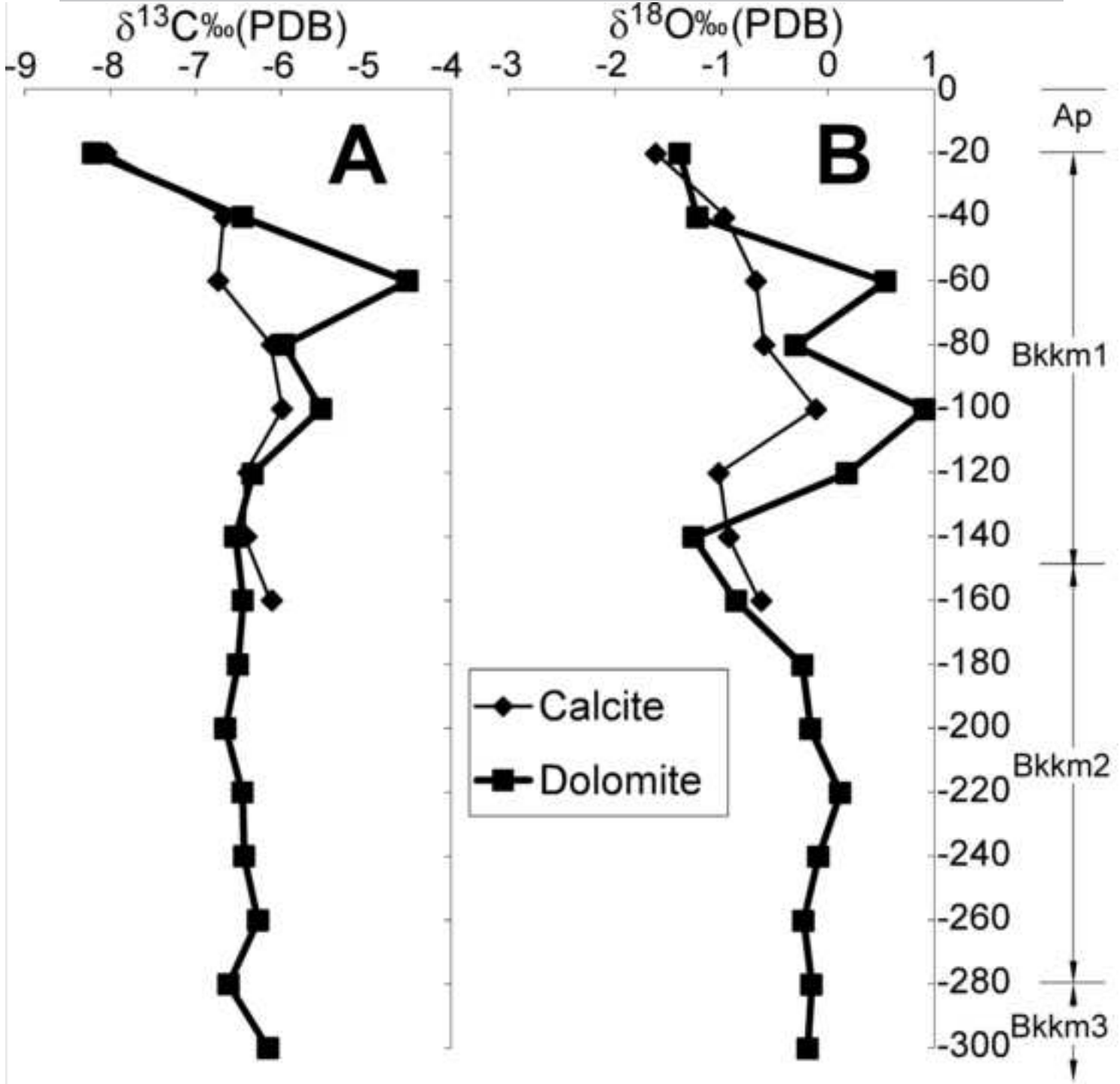

Figure 8

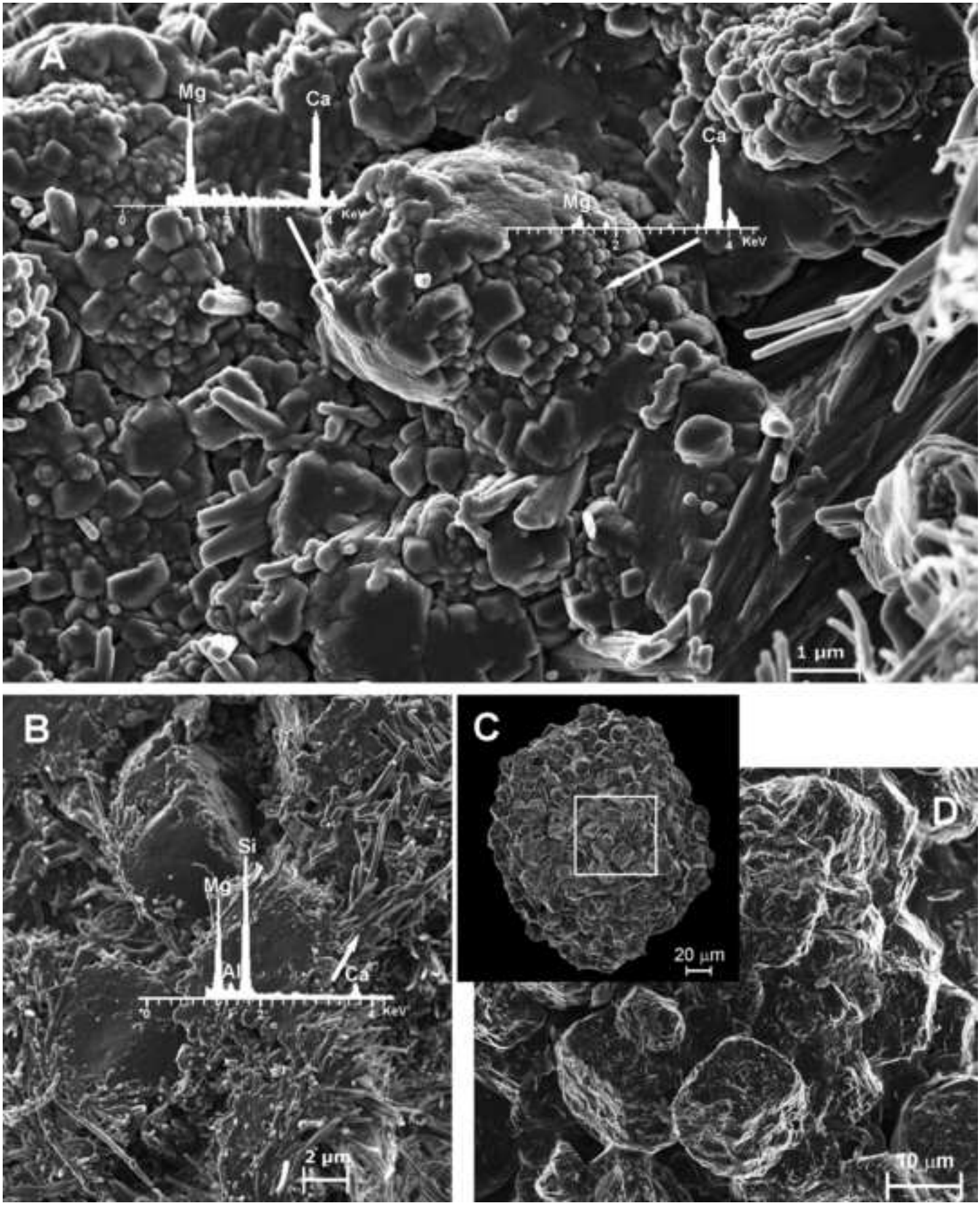

Figure 9

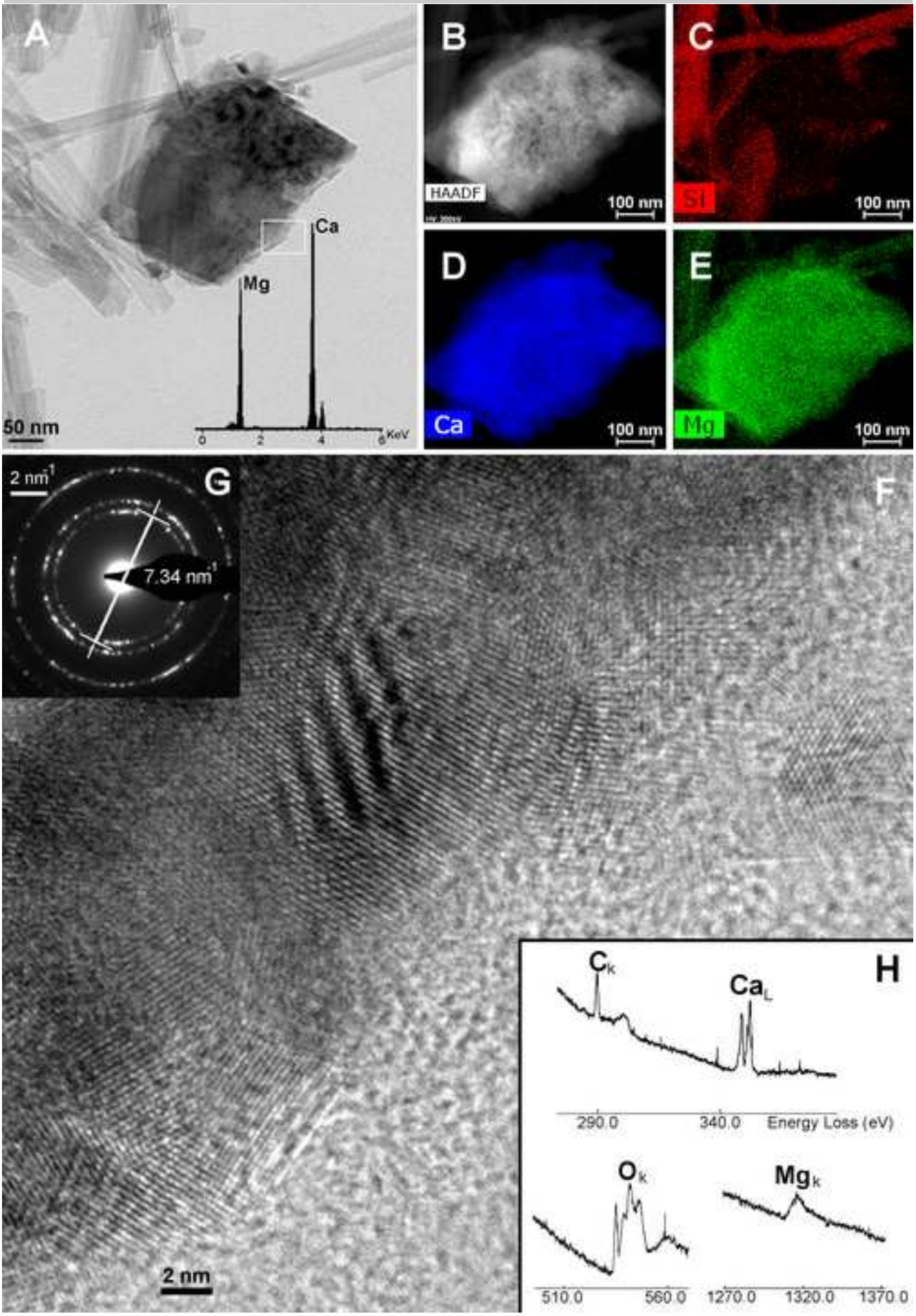

Figure 10

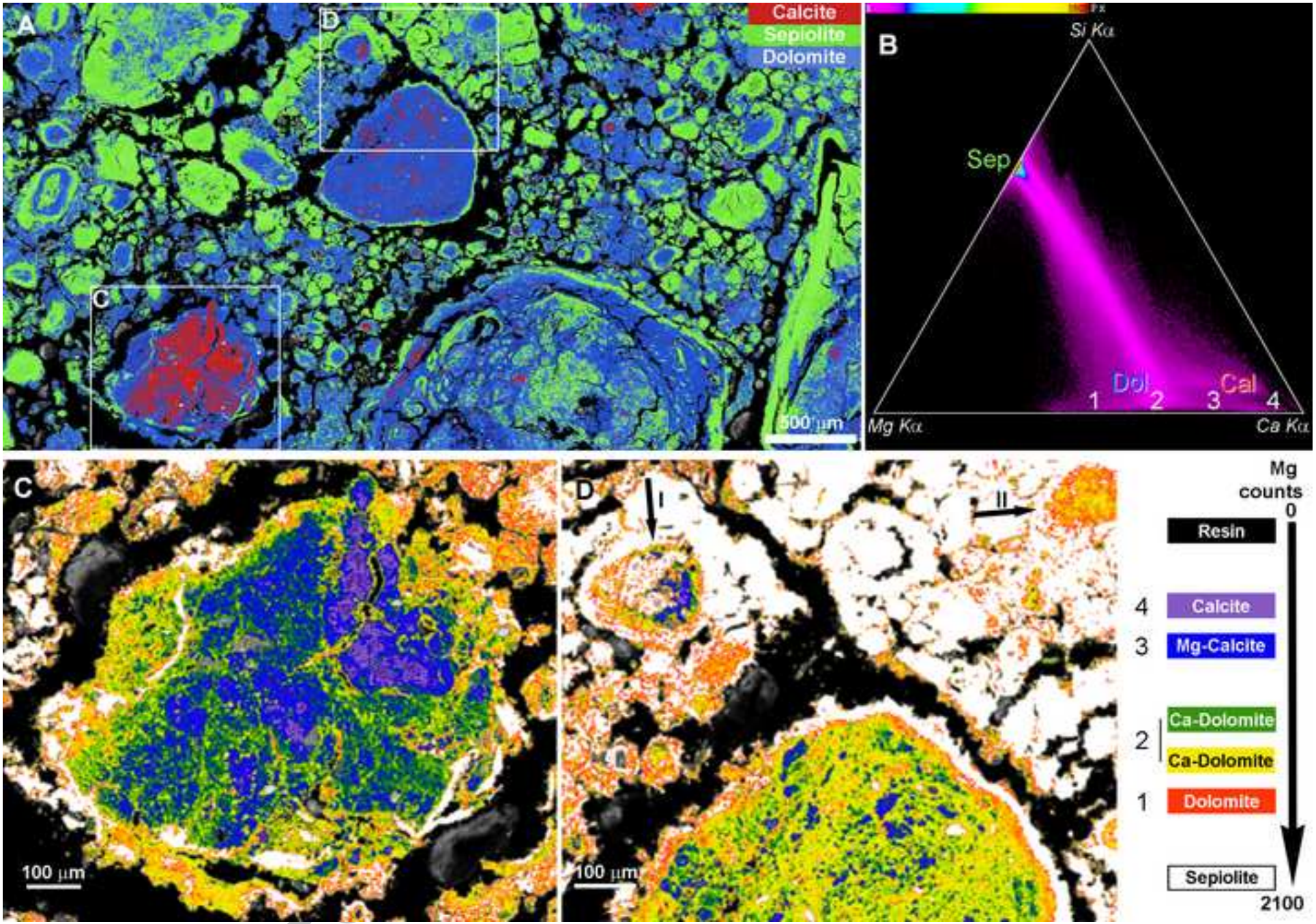

Figure 11

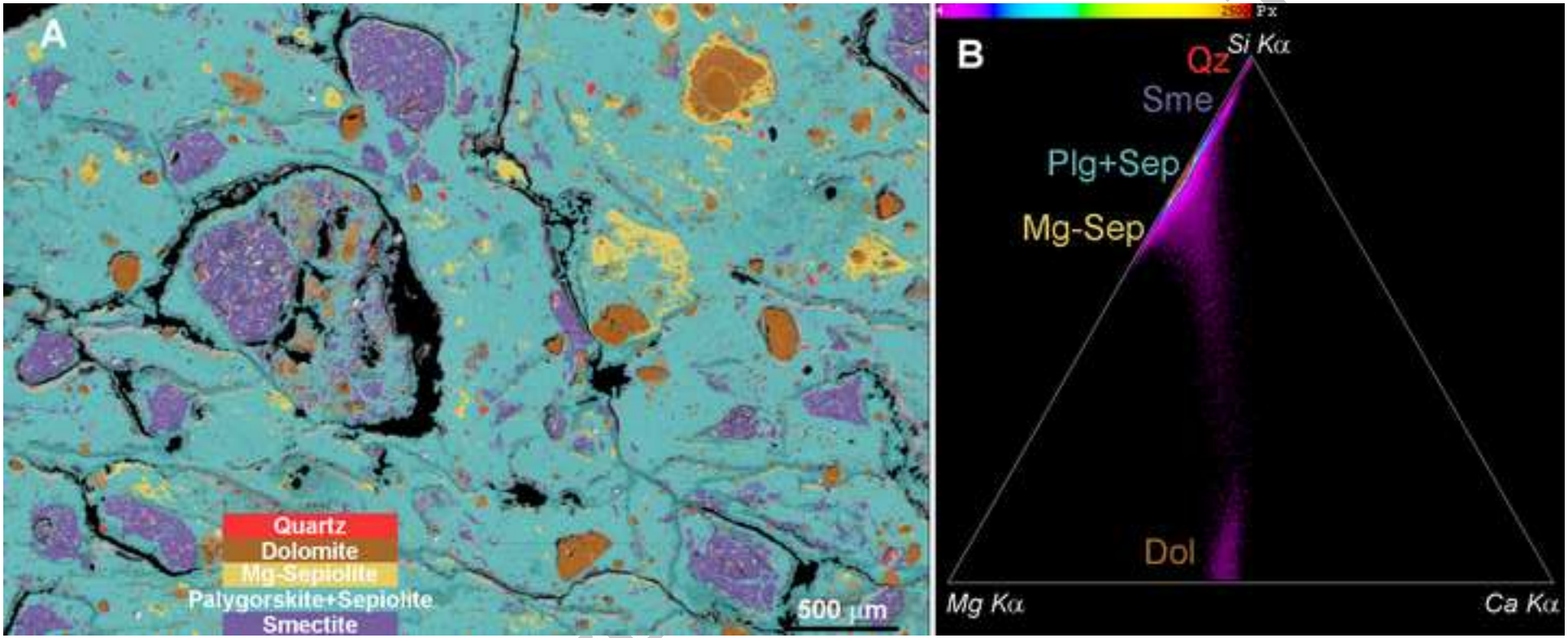

Figure 12

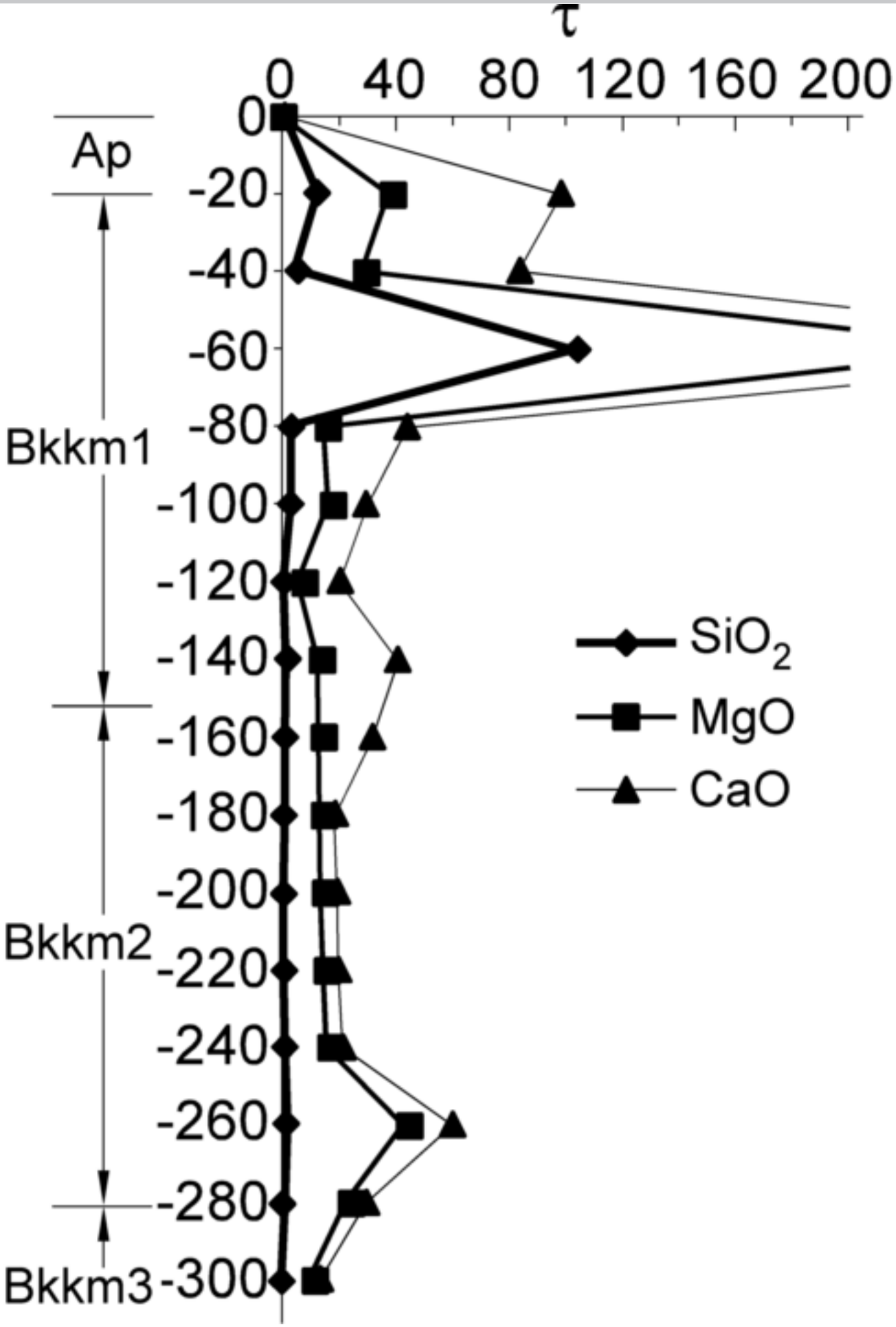

Figure 13

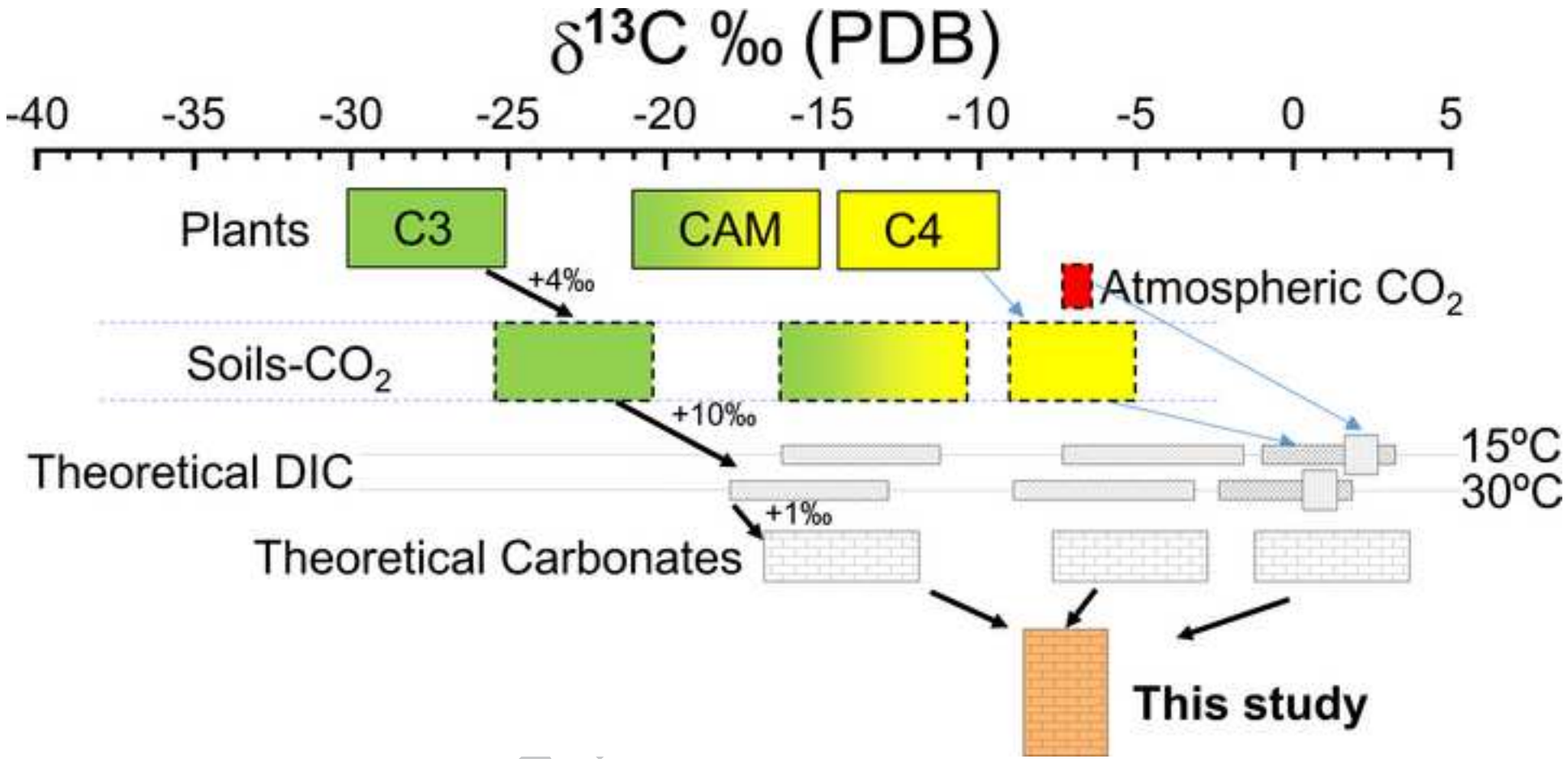

Figure 14

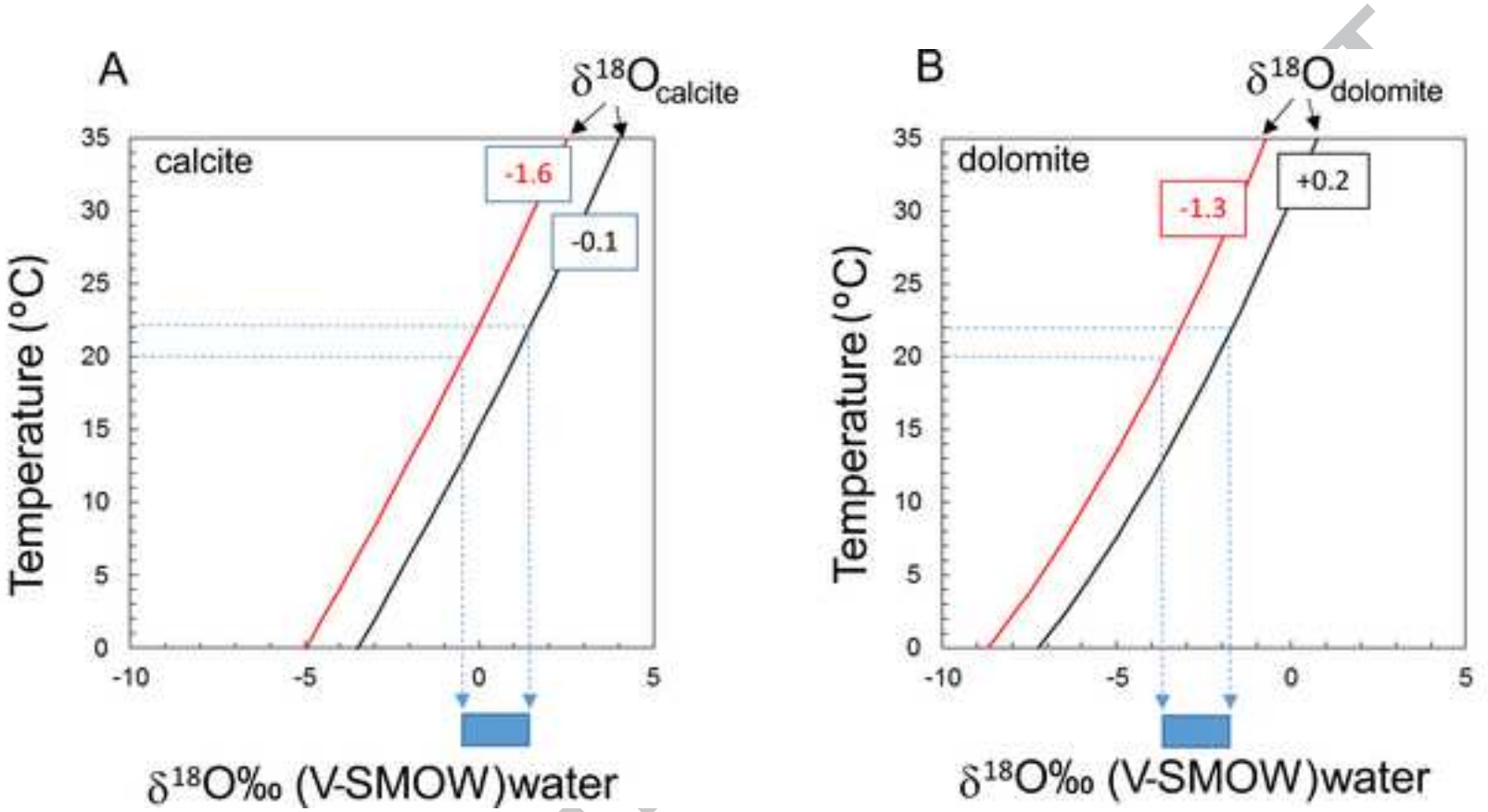

Figure 15